Reanalysis of neutron-capture elements in the benchmark r-rich star CS 31082-001

H. Ernandes, M. J. Castro, B. Barbuy, M. Spite, V. Hill, B. Castilho, C. J. Evans

Monthly Notices of the ROYAL ASTRONOMICAL SOCIETY

MNRAS **524,** 656–677 (2023) https://doi.org/10.1093/mnras/stad1764
Advance Access publication 2023 June 14

Reanalysis of neutron-capture elements in the benchmark r-rich star CS 31082−001

H. Ernandes [1,2,3★] M. J. Castro,[1] B. Barbuy,[1★] M. Spite,[4] V. Hill,[5] B. Castilho[6] and C. J. Evans[7]

[1]*Universidade de São Paulo, IAG, Rua do Matão 1226, Cidade Universitária, São Paulo 05508-900, Brazil*
[2]*Department of Astronomy and Theoretical Physics, Lund Observatory, Lund University, Box 43, SE-22100 Lund, Sweden*
[3]*Department of Geology, Lund Observatory, Sölvegatan 12, SE-22362 Lund, Sweden*
[4]*GEPI, Observatoire de Paris, PSL Research University, CNRS, Place Jules Janssen, F-92190 Meudon, France*
[5]*Université de Sophia-Antipolis, Observatoire de la Côte d'Azur, CNRS UMR 6202, BP 4229, F-06304 Nice Cedex 4, France*
[6]*Laboratório Nacional de Astrofísica, Ministério da Ciência, Tecnologia e Inovações – LNA/MCTI, R. dos Estados Unidos 154, Itajubá 37504-364, Brazil*
[7]*Space Telescope Science Institute, ESA Office, European Space Agency (ESA), 3700 San Martin Drive, Baltimore, MD 21218, USA*

Accepted 2023 June 9. Received 2023 June 9; in original form 2023 April 16

ABSTRACT

We revisit the abundances of neutron-capture elements in the metal-poor ([Fe/H] = −2.9) r-process-rich halo star CS 31082−001. Partly motivated by the development of the new near-ultraviolet Cassegrain U-band Efficient Spectrograph for the Very Large Telescope, we compiled an expanded line list for heavy elements over the range 3000–4000 Å, including hyperfine structure for several elements. Combining archival near-ultraviolet spectra of CS 31082−001 from the *Hubble Space Telescope* and the Very Large Telescope, we investigate the abundances and nucleosynthesis of 35 heavy elements (Ge, Sr, Y, Zr, Nb, Mo, Ru, Rh, Pd, Ag, Cd, Sn, Ba, La, Ce, Pr, Nd, Sm, Eu, Gd, Tb, Dy, Ho, Er, Tm, Yb, Lu, Hf, Os, Ir, Pt, Pb, Bi, Th, and U). Our analysis includes the first abundance estimates for tin, holmium, and ytterbium from these data, and the first for lutetium from ground-based data, enabling a more complete view of the abundance pattern of this important reference star. In general, the r-process-dominated elements are as enhanced as those in the Sun, particularly for elements with $Z \geq 56$ (Ba and heavier). However, the abundances for the lighter elements in our sample, from Ge to Sn ($31 \leq Z \leq 50$), do not scale with the solar abundance pattern. Moreover, the Ge abundance is deficient relative to solar, indicating that it is dominantly an iron-peak rather than neutron-capture element. Our results (or upper limits) on Sn, Pt, Au, Pb, and Bi all pose further questions, prompting further study on the origin and evolution of the known r-rich and actinide-rich, metal-poor stars.

Key words: stars: abundances – stars: atmospheres – stars: individual: BPS CS 31082−001 – Galaxy: halo.

1 INTRODUCTION

The detailed study of heavy-element stellar abundances can give us new insights into the nuclear processes that created them. In the wider context of galaxy archaeology, quantitative stellar abundances can also provide a powerful discriminator of the different phenomena contributing to nucleosynthesis. For instance, stars on the asymptotic giant branch (AGB) and spinstars (Cescutti et al. 2013; Frischknecht et al. 2016) are often associated with the synthesis of s-process elements. Meanwhile, there are several candidates for r-process enrichment, including core-collapse supernovae (SNe), magnetorotationally driven supernovae (Winteler et al. 2012; Mösta et al. 2018), jet-driven supernovae (Fujimoto, Nishimura & Hashimoto 2008; Nishimura, Takiwaki & Thielemann 2015), neutron–neutron star mergers (Abbott et al. 2017), and black hole–neutron star mergers (Just et al. 2015).

Here we revisit the neutron-capture elements in the well-studied halo star CS 31082−001, which is known to be an r-process and actinide-rich star. CS 31082−001 has a metallicity of [Fe/H] = −2.9 ± 0.1 (Hill et al. 2002), a europium enhancement of [Eu/Fe] = +1.62 (with [Ba/Eu] = −0.59), and a clear enhancement of the actinide element uranium. It is also among the brightest very metal-poor stars, with $V = 11.7$ mag.

Given its abundances, CS 31082−001 is classified as an r-II star, a class that gathers stars with [Eu/Fe] > +1.0 and [Ba/Eu] < 0.0 (Beers & Christlieb 2005). A more recent criterion of the class is a modified value of [Eu/Fe] > +0.7 (Holmbeck et al. 2020), and an interesting suggestion by Roederer, Hattori & Valluri (2018) is that stars with [Eu/Fe] > +0.7 are only found in halo-like orbits and that they were probably formed in low star formation efficiency environments such as those found in dwarf galaxies.

In a recent study, Ernandes et al. (2022, hereafter E22) employed archival near-ultraviolet (UV) spectroscopy of CS 31082−001 from ground and space observations to revisit its chemical abundances of light and iron-peak elements ($Z < 32$). This led to the first abundance estimates for Be, V, and Cu for the star and enabled new comparisons with nucleosynthesis models. Here we turn our attention to the heavy elements ($Z > 32$) in CS 31082−001.

The near-UV region is particularly rich for the study of heavy elements, making it a critical input to studies of Galactic chemical evolution and investigations of the slow and rapid neutron-capture

★ E-mail: heitor.ernandes@alumni.usp.br (HE); b.barbuy@iag.usp.br (BB)

processes and the astrophysical sites where they occur. To expand on past analyses of the heavy elements in CS 31082−001, we compiled a broader line list than in previous studies. The advantage of building on the previous works is that there are already estimated abundances for many elements, which helps to mitigate the uncertainties due to blends when extending the analysis to new lines or species. With an updated and expanded description of the elemental abundances of CS 31082−001, our objective is to investigate the predicted nucleosynthesis yields from different sources.

We add that although the near-UV region has a key role in studies of stellar nuclear processes, it is a relatively underexplored part of the spectrum. This is primarily due to the increasingly high atmospheric absorption towards shorter wavelengths from the ground, resulting in zero transmission below 3000 Å (although wavelengths below this can be accessed from space, with e.g. the *Hubble Space Telescope*, *HST*). Indeed, part of our motivation for this study is the development of the new Cassegrain U-Band Efficient Spectrograph (CUBES) instrument for the Very Large Telescope (VLT). CUBES will provide unprecedented efficiency over the spectral range of 3000–4050 Å with two spectral resolving powers ($R \sim 7000$ and $>20\,000$). Using its higher spectral resolving power, CUBES will be able to obtain near-UV spectroscopy of targets that are 2–3 mag fainter than currently possible, e.g. reaching a signal-to-noise ratio (S/N) of 20 at 3130 Å in 1 h of exposure for an A0-type star with $U = 17.5$ mag. (Cristiani et al. 2022). This will bring an exciting new capability for studies of metal-poor stars similar to CS 31082−001.

The archival spectra used in the analysis are summarized briefly in Section 2, with the analysis and previous results discussed in Section 3. The heavy elements studied are detailed in Section 4, including the relevant calculations and fitting methods, with a discussion of the results in Section 5, and our conclusions in Section 6. Supporting material is given in the appendices, including the near-UV line list of the heavy elements studied in CS 31082−001, and simulated CUBES observations of two illustrative heavy-element lines in its spectrum.

2 OBSERVATIONS

To investigate the heavy-element lines in CS 31082−001 we used the same near-UV spectra as in E22, which were obtained with the Ultraviolet and Visual Echelle Spectrograph (UVES; Dekker et al. 2000) at the VLT in 2000 August and October in the 'First Stars' programme (ID: 165.N-0276(A), PI: R. Cayrel). Here we employ the spectra observed with central wavelengths of 3400 Å, which covers the 3000–3850 Å range, and the spectra centred at 4370 Å, covering 3770–4990 Å (Hill et al. 2002). As in E22, the three spectra observed at the 3400 Å setting were combined, giving an S/N of 100 at 3400 Å, and 20 at 3070 Å (Spite et al. 2005; Barbuy et al. 2011; Siqueira-Mello et al. 2013).

For first estimates, we derived all abundances from a smoothed spectrum [full width at half-maximum (FWHM) ≈ 0.09 Å]. To then estimate the error in the line fitting and choice of continuum, we fitted all the lines in the raw (unsmoothed) data, which have an FWHM ≈ 0.06–0.08 Å. Where possible, the initial fits adopted the previous abundances collated by E22, and for this reason the values can appear very specific; for example, $A(\mathrm{Y}) = -0.23$, which when also computed with ±0.2, gives −0.03 and −0.43.

A further check was carried out using spectra observed at the Keck telescope with the High Resolution Echelle Spectrometer (HIRES; Sneden et al. 2009), where we retrieved and combined the blue orders from the observations that overlap with the wavelength range of our selected UVES data. After summing the observations for each order and normalizing them, we combined the orders together for a final spectrum (enabled by the overlap of ∼5 Å between each order and because the HIRES spectra have the same rebinned wavelength sampling as the UVES data).

Table 1. Summary of observations used in this study. Columns are the spectral resolving power (R), the mean signal-to-noise ratio (S/N) per rebinned pixel, the wavelength range, the program identifiers (ID), and Principal Investigator (PI).

Instrument	R	S/N	λ range (Å)	ID	PI
VLT-UVES	42 000	150	3020–3810	165.N-0276	R. Cayrel
VLT-UVES	47 000	350	3730–4993	165.N-0276	R. Cayrel
Keck-HIRES	40 000	150	3201–4718	U53H	M. Bolte
HST-STIS	30 000	40	2680–3070	9359	R. Cayrel

For lines near the ground atmospheric UV cut-off (i.e. 3000–3070 Å) we also use spectra from the *HST* Space Telescope Imaging Spectrograph (STIS) with the E230M grating (see Barbuy et al. 2011), from which we use the data from order 2 (3012–3070 Å) and order 3 (2980–3025 Å).

Details of the observations analysed in this work are summarized in Table 1, including spectral resolving power (R), mean S/N per pixel,[1] wavelength range, program identifiers, and Principal Investigator (PI).

The reduced UVES data analysed here were reprocessed by ESO in their archive in 2020. These reductions include several developments compared to the UVES data analysed in previous papers. When the MIDAS version of the pipeline was ported to the ESO Common Pipeline Library (CPL), an important step was the implementation of a proper optimal extraction. Additional improvements included order tracing, robustness to bad pixels (in particular column traps affecting one of the two chips) and enabling successful extractions even when one order lacks a signal (interpolating the results from traces on adjacent orders), and improved calibration of spectral response and flux (see Larsen et al. 2007). The pipeline was further upgraded for implementation in the EsoReflex environment (Freudling et al. 2013).

3 ABUNDANCE ANALYSIS

For the abundance analysis we used the TURBOSPECTRUMcode from Alvarez & Plez (1998) and Plez (2012) to generate the synthetic spectra. For stellar parameters we adopted ($T_{\rm eff}$, $\log g$, [Fe/H], $v_{\rm t}$) = (4825 ± 50 K, 1.5 ± 0.3, −2.9 ± 0.1, 1.8 ± 0.2 km s^{-1}) from Hill et al. (2002). Model atmosphere grids are from Gustafsson et al. (2008).

The list of lines of heavy elements, together with oscillator strengths from Kurucz (1993),[2] and the Vienna Atomic Line Database (VALD; Piskunov et al. 1995; Ryabchikova et al. 2015),[3] are given in Table A1. The wavelengths are mostly from Kurucz (1993).

Compared to previous analyses, we highlight the inclusion of Ho II and Yb II. We also added more lines for other elements to extend the line list, and checked these one-by-one if they were too faint or blended to be useful (see comments in Section 4). We were able to include lines for: Ge, Sr, Y, Zr, Nb, Mo, Ru, Rh, Pd, Ag, (Cd),[4] Sn,

[1] Calculated with http://www.stecf.org/software/ASTROsoft/DER_SNR/
[2] http://kurucz.harvard.edu/atoms.html
[3] http://vald.astro.uu.se/
[4] Unfortunately the single Cd I line in the near-UV region is too weak to derive an elemental abundance.

Table 2. Summary of heavy-element abundances for CS 31082−001 derived in this study, $A(X)_{present}$ and $[X/Fe]_{present}$, compared to those from previous works as follows: [1]Hill et al. (2002), [2]Plez et al. (2004), [3]Barbuy et al. (2011), [4]Siqueira-Mello et al. (2013), and [5]Sneden et al. (2009). Solar abundances in the third column are adopted from Asplund et al. (2021). The uncertainties ($\sigma_{[X/Fe]}$) are computed considering the statistical (σ_{fit}) and systematic uncertainties that come from the fit of the number of lines (N) for each element, where the systematic uncertainties come from the stellar parameters (column 3) and the derivations from the UVES spectra (column 10). Notation '1st ∗s' means 'First Stars'.

Element	Z	$A(X)_{\odot\,adopted}$	$A(X)_{VLT,\,Keck}$ [1st∗s]	$A(X)_{HST}$ [1st∗s]	N	$A(X)_{present}$	$[X/Fe]_{present}$	$\sigma_{\sqrt{fit^2+param^2}}$
Ge	32	3.62	...	+0.10[4]	1	0.48	−0.24	0.16
Sr	38	2.83	+0.72[1]	...	2	0.55	0.62	0.16
Y	39	2.21	−0.23[1], −0.15[4]	...	22	−0.37	0.32	0.21
Zr	40	2.59	+0.43[1]	+0.55[4]	66	0.26	0.57	0.19
Nb	41	1.47	−0.55[1]	−0.52[4]	3	−0.65	0.78	0.14
Mo	42	1.88	...	−0.11[4]	1	−0.21	0.81	0.09
Ru	44	1.75	+0.36[1]	+0.65[4]	5	0.18	1.33	0.16
Rh	45	0.78	−0.42[1, 4]	...	3	−0.51	1.61	0.19
Pd	46	1.57	−0.05[1], −0.09[4]	...	5	−0.21	1.12	0.18
Ag	47	0.96	−0.81[1], −0.84[4]	...	2	−0.94	1.00	0.18
Sn	50	2.02	...	...	1	<−0.40	<0.48	0.22
Ba	56	2.27	+0.40[1]	...	1	0.40	1.03	0.15
La	57	1.11	−0.60[1], −0.60[5]	...	6	−0.73	1.06	0.15
Ce	58	1.58	−0.31[1, 4], −0.29[5]	...	18	−0.41	0.91	0.16
Pr	59	0.75	−0.86[1], −0.79[5]	...	3	−0.94	1.21	0.12
Nd	60	1.42	−0.13[1], −0.21[4], −0.15[5]	...	24	−0.33	1.15	0.15
Sm	62	0.95	−0.51[1], −0.42[4, 5]	...	26	−0.54	1.41	0.22
Eu	63	0.52	−0.76[1], −0.72[5]	−0.75[4]	6	−0.93	1.45	0.14
Gd	64	1.08	−0.27[1], −0.21[5]	−0.22[4]	39	−0.45	1.37	0.16
Tb	65	0.31	−1.26[1], −1.01[5]	−0.50[4]	11	−1.22	1.37	0.15
Dy	66	1.10	−0.21[1], −0.12[4], −0.07[5]	...	28	−0.25	1.55	0.14
Ho	67	0.48	−0.80[5]	...	3	−0.98	1.44	0.15
Er	68	0.93	−0.27[1], −0.30[5]	−0.20[4]	21	−0.38	1.59	0.17
Tm	69	0.11	−1.24[1], −1.18[4], −1.15[5]	...	10	−1.32	1.47	0.20
Yb	70	0.85	−0.41[5]	...	2	−0.70	1.35	0.21
Lu	71	0.10	...	...	2	−1.14	1.66	0.08
Hf	72	0.85	−0.59[1], −0.73[4], −0.72[5]	...	6	−0.88	1.17	0.09
Ta	73	−0.15	...	−1.60[4]	...	...	1.45	...
W	74	0.79	...	−0.90[4]	...	...	1.21	...
Re	75	0.26	...	−0.21[4]	...	...	2.43	...
Os	76	1.35	+0.43[1]	−0.07[4]	3	0.23	1.78	0.22
Ir	77	1.32	+0.20[1]	+0.18[4]	5	0.10	1.68	0.18
Pt	78	1.61	...	+0.30[3]	2	0.00	1.29	0.30
Au	79	0.91	...	−1.00[3]	1	−1.39	0.60	0.16[2]
Pb	82	1.95	−0.55[2]	−0.65[3]	1	−0.65	0.30	...
Bi	83	0.65	...	−0.40[3]	1	−0.20	2.05	0.28
Th	90	0.03	−0.98[1]	...	6	−1.04	1.83	0.10
U	92	−0.54	−1.92[1]	...	1	−1.92	1.52	0.14

Ba, La, Ce, Pr, Nd, Sm, Eu, Gd, Tb, Dy, Ho, Er, Tm, Yb, Lu, Hf, Os, Ir, Pt, (Pb),[5] Bi, Th, and U. A blended line of Sn can be used with uncertainties.

We present our estimated abundances for CS 31082−001 from the expanded line list in Table 2; these include the first estimates of Sn, Ho, and Yb from these data, as well as for Ba and Lu from analysis of the ground UV lines. In the table we also compile previous abundance estimates for the neutron-capture elements from Hill et al. (2002), Plez et al. (2004), Barbuy et al. (2011), and Siqueira-Mello et al. (2013), as given by E22 and Sneden et al. (2009). Solar abundances from Asplund et al. (2021) are also given in the third column of the table. We note that the latter are somewhat different from the solar abundances adopted by Hill et al. (2002), which were from Grevesse & Sauval (1998).

[5]The two Pb I lines in this region are not sensitive enough to derive an elemental abundance. Therefore, we adopted the results from Plez et al. (2004) and Siqueira-Mello et al. (2013).

3.1 Hyperfine structure: summary

Some of the heavy elements that we investigate here present hyperfine structure (HFS), which we now describe briefly in turn.

(i) *Barium*: for the unique Ba II line available in the ground UV we computed the HFS.

(ii) *Lanthanum*: the HFS shifts for La II lines are given by Lawler, Bonvallet & Sneden (2001a), and they are available in the VALD line lists.

(iii) *Cerium*: according to Lawler, Sneden & Cowan (2009), there is no need to include the HFS for Ce II because the main isotopes are even with nuclear spin $I = 0$.

(iv) *Praseodymium*: HFS from Sneden et al. (2009) is included in VALD.

(v) *Samarium*: HFS constants A and B on ^{147}Sm II and ^{149}Sm II are given by Masterman et al. (2003), and some more information is given by Lundqvist, Wahlgren & Hill (2007). However, we were unable to find the configuration of upper levels in Kurucz (1993) nor in the National Institute of Standards and Technology (NIST) or VALD line lists. Furthermore, the 147 and 149 isotopes correspond to 14.99 per cent and 13.82 per cent of the six isotopes in the Solar system mixture, which are dominated by the even atomic numbers (Asplund et al. 2009). Therefore, we did not apply HFS for the Sm lines here, and the effect would probably be negligible.

(vi) *Europium*: we computed the HFS for the relevant lines as they were not available in VALD.

(vii) *Terbium*: the HFS splitting is given by Lawler et al. (2001c) and Lawler, Wyart & Blaise (2001d) and for many of the lines they are included in VALD. For four lines, not available in VALD, we computed the HFS adopting the log gf values from Lawler et al. (2001c). Lawler et al. (2009) also gave the HFS splitting for these lines.

(viii) *Dysprosium*: the isotopes $^{160,\,161,\,162,\,163,\,164}$Dy II correspond to 2.33 per cent, 18.89 per cent, 25.48 per cent, 24.90 per cent, and 28.26 per cent, respectively, of the element constitution in the Solar system mixture. Constants A and B are given by Del Papa, Holt & Rosner (2017). However, as with Sm, the upper level configuration is not identified for most lines. Therefore, we could not apply the HFS for the Dy II lines, even though in this case the odd atomic number isotopes amount to close to 50 per cent of the element.

(ix) *Holmium*: HFS is critical for Ho II, and is available from Lawler, Sneden & Cowan (2004).

(x) *Ytterbium*: HFS for Yb II lines was adopted from Sneden et al. (2009).

(xi) *Lutetium*: HFS from Den Hartog, Lawler & Roederer (2020) is included in VALD.

(xii) *Osmium*: HFS does not show a significant contribution to the line profile for Os, as described by Cowan et al. (2005).

(xiii) *Platinum*: HFS is adopted from Den Hartog et al. (2005) for the two lines.

3.2 Hyperfine structure: calculations

The HFS calculations for the Ba II, Eu II, and Tb II lines were carried out using the code developed by McWilliam, Wallerstein & Mottini (2013) adopting the constants A and B from Rutten (1978) and Lawler et al. (2001b), respectively. In cases that the B constant is not provided, we adopted $B = 0.0$.

The Ba II line identified in the region needs to have HFS taken into account, which is not included in VALD. We adopted atomic constants from Rutten (1978). McWilliam (1998) reports HFS splitting for several Ba II lines. We adopt the solar mixture isotopic fractions of 40 per cent, 32 per cent, and 28 per cent for ^{135}Ba, ^{137}Ba, and ^{138}Ba, respectively. The HFS splitting in this case is in fact negligible. We also caution that, as extensively discussed by McWilliam (1998), the isotopic fractions could be different in old stars such as CS 31082−001, because probably no s-process contribution took place and all neutron-capture elements would have been formed by the r-process. That said, it could also be that spinstars could be responsible for forming neutron-capture elements through the s-process.

To analyse the Eu II spectral lines with enough accuracy it is necessary to include the HFS, especially the transitions that include the ground configuration such as the 3688.430, 3724.930, and 3819.672 Å lines. We have computed the HFS shift for the Eu II lines that were not included in the VALD line lists. Eu has two stable isotopes, ^{151}Eu and ^{153}Eu, in the proportion of 47.9 per cent and 52.2 per cent in the solar mixture, respectively. The nuclear spin for both isotopes of Eu II (151 and 153) is $I = 5/2$. We verified that our calculations of HFS based on the code by McWilliam et al. (2013) are very similar to the HFS line splitting and respective log gf from Ivans et al. (2006).

As noted above, most of the HFS for the selected Tb II lines are available in VALD. We have computed the HFS for four lines that were not included in the VALD line list: Tb II 3509.144, 3633.287, 3641.655, and 3899.188 Å. The HFS calculations for these Tb II lines are somewhat simpler than for other elements given that Tb only has one isotope, ^{159}Tb with a nuclear spin of $I = 3/2$. The constants, energy levels, and log gf values for these line transitions were adopted from Lawler et al. (2001c,d). We verified that the line splitting from our computations, using the code by McWilliam et al. (2013) and the constants from Lawler et al. (2001c), is very similar to those given by Lawler et al. (2009).

4 COMMENTS ON LINES

The abundance estimates for all lines were derived from close inspection of each feature. We now discuss each element in turn. We note that, within the quoted uncertainties, the present results are generally compatible with previous results from Hill et al. (2002), Sneden et al. (2009), Barbuy et al. (2011), and Siqueira-Mello et al. (2013). Where small differences occur these can generally be explained by either the continuum placement and/or the adopted FWHM for convolution of the spectra in the analysis.

4.1 Germanium

The single line of Ge I 3039.067 Å is well fitted with A(Ge) = 0.45–0.51, as shown in Fig. 1, therefore we adopt A(Ge) = 0.48. The fits in the figure are for the following spectra: *HST*-STIS (order 2), UVES smoothed, UVES raw (from the 2020 archival reductions), and UVES raw from the previous reductions. The lower value of A(Ge) = 0.10 found by Siqueira-Mello et al. (2013) could be due to a different continuum placement and convolution, given that the line is weak.

4.2 Strontium

In Fig. 2, we show the fit of the near-UV and traditional diagnostic lines of Sr I and Sr II. The analysis of Sr is difficult because it has only a few useful lines in the near-UV. The Sr II 3464.453 and 3474.889 Å lines appear too strong using the value of A(Sr) = 0.72 from Hill et al. (2002), and are well fitted with A(Sr) = 0.40. The Sr II 3474.889 Å line is weak and the Sr II 3464.453 Å line is potentially a suitable diagnostic line, except that its log gf value is indicated in NIST as not precise, as well as having a blend with a Sm II line (for which we adopted our derived value of A(Sm) = −0.54 to investigate the blend).

The lines employed by Hill et al. (2002) were more traditional for the derivation of the Sr abundance: Sr II 4077.709, 4161.792, and 4215.519 Å. We confirmed that these lines give a Sr abundance of A(Sr) = 0.70, including also the Sr I 4607.33 Å line. We therefore adopted a mean value between the UV lines and the lines near 4000 Å, of A(Sr) = 0.55. Note that for Sr II 4077.709 Å we adopted the revised log gf = 0.148 from Roederer et al. (2022b). Fig. 2 shows the fits to all the Sr lines considered.

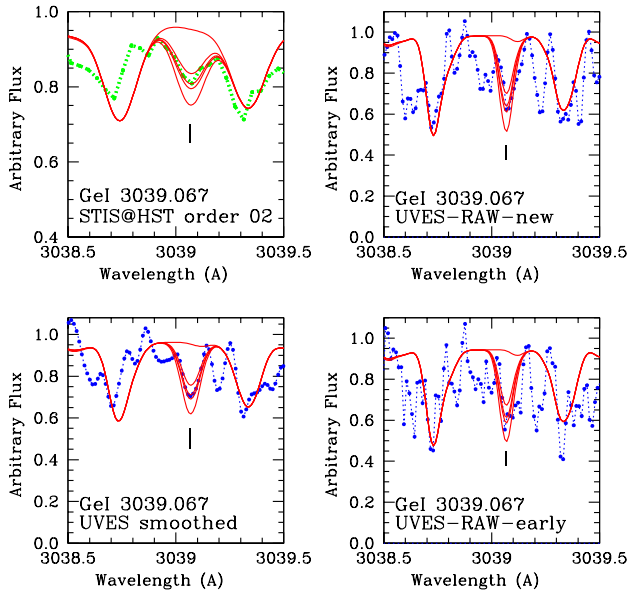

Figure 1. Fits to the Ge I 3039.067 Å line for the *HST*-STIS and UVES spectra, plotted in green and blue, respectively. The smoothed UVES data are shown in the lower left-hand panel, the newly reduced data in the upper right-hand panel, and the previous reductions in the lower right-hand panel. Synthetic spectra (red lines) are shown for A(Ge) = none, 0.71, 0.51, 0.45, and 0.31. A(Ge) = 0.51 corresponds to [Ge/Fe] = 0.

4.3 Yttrium

The 22 Y II lines give a mean of A(Y) = −0.37 ± 0.17. This is compatible with the result of A(Y) = −0.23 from Hill et al. (2002), who had four lines in common with our analysis, as well as six further lines in the 4300–5300 Å region.

4.4 Zirconium

The 72 Zr II lines give a mean of A(Zr) = 0.33 ± 0.15, somewhat lower than the previous values of A(Zr) = 0.43 from Hill et al. (2002) and A(Zr) = 0.55 from Siqueira-Mello et al. (2013).

Given that the higher value from Siqueira-Mello et al. (2013) was derived from the STIS spectra, we inspected the Zr II lines they used, which are in STIS orders 4, 5, 6, 7, 9, 10, and 11. Most of the lines in the region 2600–3000 Å are blended and not very sensitive to the Zr abundance; the more reliable lines are Zr II 2916.626 Å and Zr II 2962.673 Å that give A(Zr) = 0.43 and 0.33, respectively.

Taking into account the 72 lines, including the two best lines in the extended STIS region, we obtain a mean value of A(Zr) = 0.33 ± 0.15.

4.5 Niobium

The Nb II 3028.433 Å line, located at the edge of the STIS order 2 spectrum, is noisy. The region was approximately fit, but the line itself appears in the calculation as a blend with the next line shortwards of it, giving problems with fitting the continuum level as well.

For other lines, Nb II 3191.093 Å is fitted with A(Nb) = −0.75 and Nb II 3215.591 Å with A(Nb) = −0.65 (close to A(Nb) = −0.55 from Hill et al. 2002). Nb II 3225.475 Å appears as a strong line, possibly due to blends and was therefore not taken into account in the mean. From these considerations, we adopt A(Nb) = −0.65.

4.6 Molybdenum

The unique Mo I 3864.103 Å is well fitted with A(Mo) = −0.21, close to the previous value of A(Mo) = −0.11 ± 0.13 from three lines in the STIS region by Siqueira-Mello et al. (2013). Note that this line is blended with a CN feature, but in this star the CN lines are weak.

4.7 Ruthenium

The Ru I 3436.736, 3498.942, and 3728.025 Å lines are well fitted with A(Ru) = 0.15–0.20. The lines at 3798.898 and 3799.349 Å are weak and blended, but also compatible with A(Ru) = 0.20. We also inspected the Ru I 2874.988 Å line observed with STIS that, although very weak, is compatible with A(Ru) = 0.25. We therefore adopt A(Ru) = 0.18 from the five lines in Table A1, which is compatible with A(Ru) = 0.36 from Hill et al. (2002) within the uncertainties (see Table 1), and lower than the result of A(Ru) = 0.65 from Siqueira-Mello et al. (2013).

4.8 Rhodium

Rh I 3396.819 and 3700.907 Å are rather weak and on the bluewards wing of stronger lines, but are well fitted with A(Rh) = −0.62 and −0.42, respectively, whereas Rh I 3434.885 Å gives A(Rh) = −0.57. The Rh I 3692.358 Å line is weak and on the redwards wing of a stronger (unidentified) line, and is compatible with A(Rh) = −0.42. A mean value of A(Rh) = −0.51 ± 0.09 is close to the abundance of A(Rh) = −0.42 from Hill et al. (2002).

4.9 Palladium

The five lines give a mean of A(Pd) = −0.21 ± 0.07, somewhat lower than the value of A(Pd) = −0.05 from Hill et al. (2002). There is good line-by-line agreement between the estimates from the raw (non-smoothed) UVES and Keck spectra.

4.10 Silver

The two lines give a mean of A(Ag) = −0.94 ± 0.07, in very good agreement with A(Ag) = −0.95 from Hill et al. (2002), and compatible with the value A(Ag) = −1.03 from Siqueira-Mello et al. (2013). The results from the smoothed and raw UVES data and the Keck spectra are all very similar.

4.11 Cadmium

The sole Cd line is hardly detectable, and moreover, is immersed within OH lines. Only a very small change in the feature takes place by changing its abundance by 0.2 dex, and therefore the Cd abundance cannot be derived.

4.12 Tin

The one Sn I line, at 3262.331 Å, is blended with Sm II 3262.27 Å and Os I 3262.29 Å, as pointed out by Sneden et al. (2003) and shown in Fig. 3. The blend is well fitted with A(Os) = 0.0 (where the Os line is the stronger feature), A(Sm) = −0.51, and A(Sn) = −0.40 or [Sn/Fe] = +0.5. We add though that the Sn abundance in Sn I 3262.331 Å has a small impact in the overall feature, so we only adopted an upper limit on the Sn abundance of A(Sn) < −0.40. Sn is mostly produced by the s-process in the solar mixture, and in

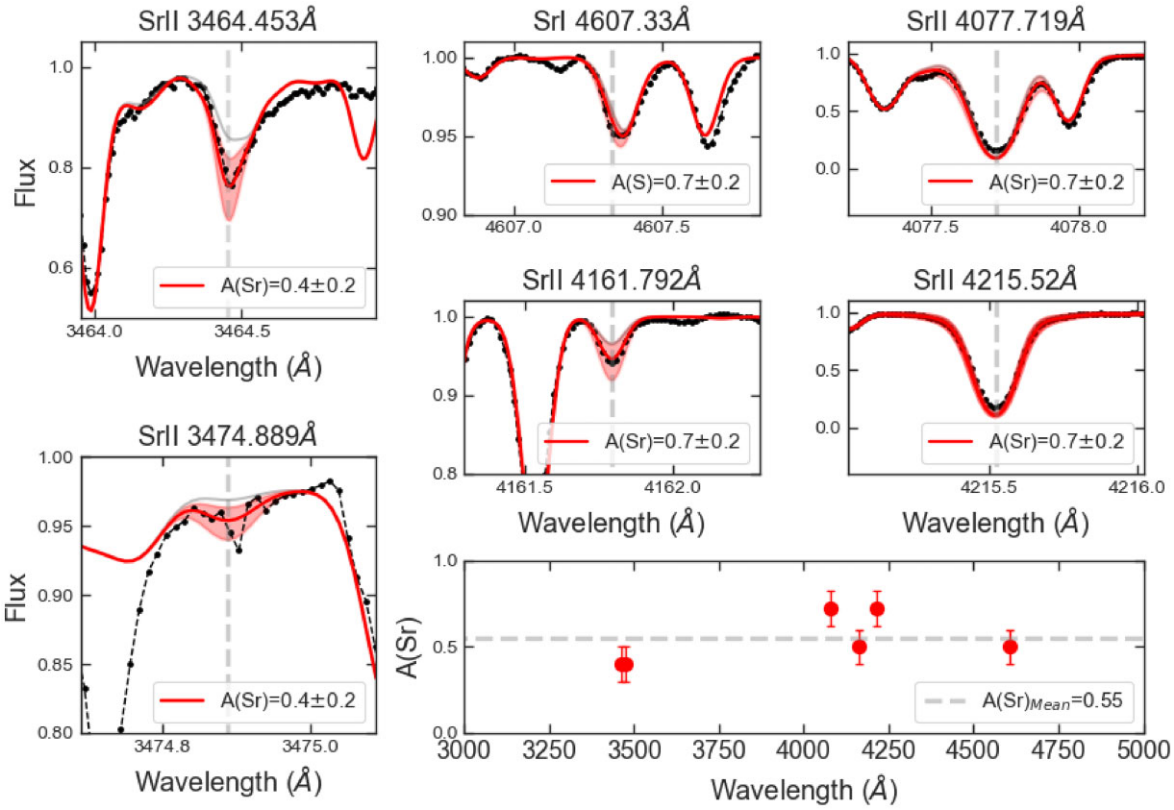

Figure 2. Fits to the Sr II lines. Sr II 3464.453 and 3474.889 Å (left-hand panels) are well fitted with $A(\mathrm{Sr}) = 0.40$ (red lines). The Sr II 4077.709, 4161.792, and 4215.519 Å lines are well fitted with $A(\mathrm{Sr}) \sim 0.70$. The UVES spectrum is shown in black, the shaded red areas indicate an abundance variation of ±0.2, and the grey line represents $A(\mathrm{Sr}) =$ none. The lower horizontal panel shows the mean abundance (dashed line) from the six lines, with the variation between lines within the error bars showing systematic uncertainties of $\sigma_{\mathrm{parm}}(\mathrm{Sr}) = 0.1$.

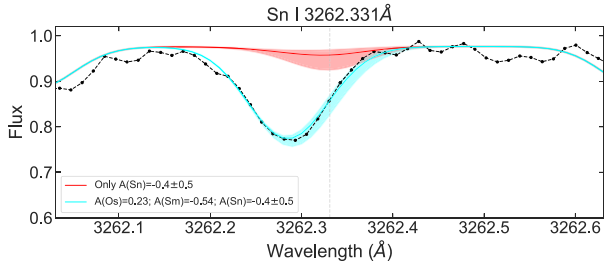

Figure 3. Fit to the Sn I 3262.331 Å line that includes calculations with $A(\mathrm{Sn}) = -0.90$, −0.40, −0.20, and 0.0. The red region shows the models including only Sn, while the cyan region includes blending from Os and Sm, with $A(\mathrm{Os}) = 0.0$ and $A(\mathrm{Sm}) = -0.51$, respectively.

CS 31082−001 it is probably produced in a small contribution from the r-process, which in principle explains that this element is not much enhanced in this star. There are two other Sn lines in this region, but they are undetectable – the Sn I 3655.790 Å line has its feature strongly overlapping with a Ce II line, while the 3801.011 Å line is too weak and so presents no detectable feature for $A(\mathrm{Sn}) = -0.40$.

4.13 Barium

The sole useful Ba II line is at 3891.776 Å and is blended with a Fe I line. This is well fitted with $A(\mathrm{Ba}) = 0.15$, as shown in Fig. 4, where we also show fits to more traditional Ba lines in the range 4000–5000 Å, i.e. Ba II 4130.645, 4554.229, and 4934.076 Å. A mean value of $A(\mathrm{Ba}) = 0.40$ is obtained, in agreement with the mean value from Hill et al. (2002).

4.14 Lanthanum

The mean of the six lines gives $A(\mathrm{La}) = -0.73 \pm 0.07$, only somewhat lower than $A(\mathrm{La}) = -0.60$ from Hill et al. (2002). The results from fits with the three sets of spectra are all very similar.

4.15 Cerium

The 19 lines give a mean of $A(\mathrm{Ce}) = -0.41 \pm 0.11$, only slightly lower than $A(\mathrm{Ce}) = -0.31$ from Hill et al. (2002). The exceptions are the Ce II 3263.885 and 3984.671 Å lines that are not well fitted due to blends and these lines were therefore not considered. The Ce II 3999.237 Å line was only used in the case of the raw (non-smoothed) UVES spectrum.

4.16 Praseodymium

The triplet lines are well fitted by a mean of $A(\mathrm{Pr}) = -0.94 \pm 0.02$, close to the value of $A(\mathrm{Pr}) = -0.86$ from Hill et al. (2002).

4.17 Neodymium

A mean of $A(\mathrm{Nd}) = -0.33 \pm 0.09$ is found from 23 lines, somewhat lower than the abundance of $A(\mathrm{Nd}) = -0.13$ from Hill et al. (2002). The exceptions are Nd II 3285.085 Å, which is faint and just

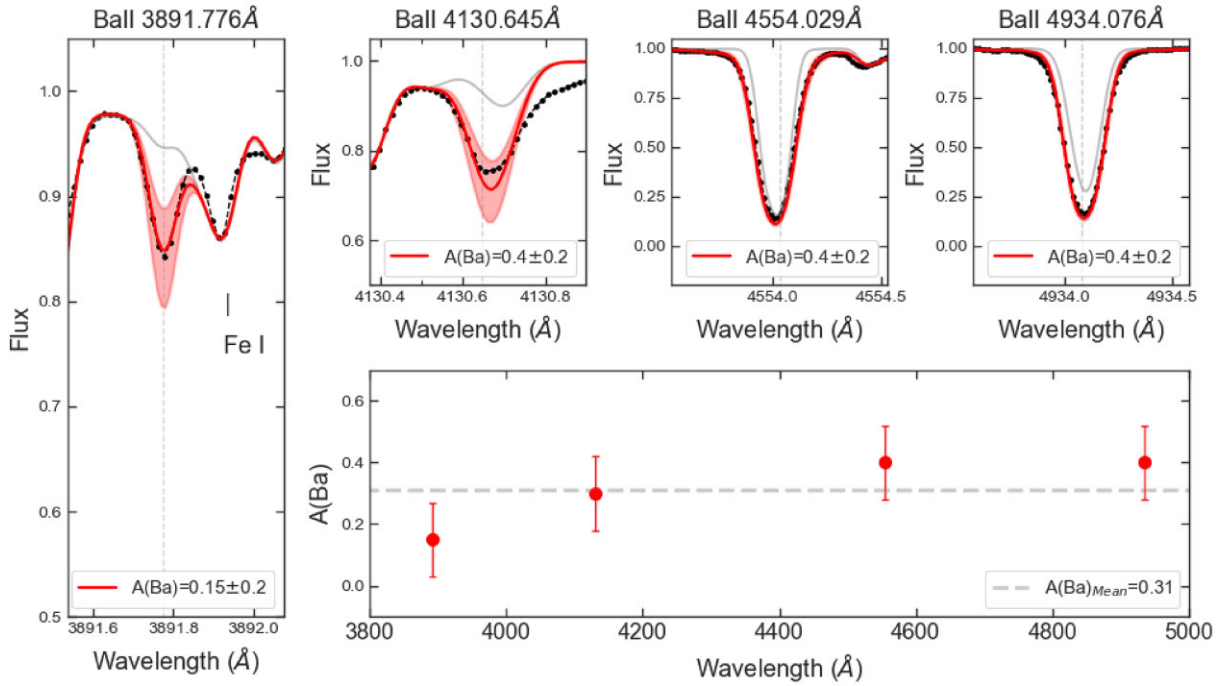

Figure 4. Fits to the Ba II 3891.776 Å line in the near-UV and to the more traditional optical Ba II 4130.645, 4554.229, and 4934.076 Å lines. The UVES spectrum is shown in black, the shaded red areas indicate an abundance variation of ±0.15, and the grey line represents A(Ba) = none. The lower horizontal panel shows the mean abundance (dashed line) from the four lines, with the variation between lines with the error bars showing systematic uncertainties of $\sigma_{\rm parm}$(Ba) = 0.12.

longwards of a stronger line (with a fit to the blended feature giving a lower Nd abundance of A(Nd) = −0.53), and Nd II 3334.465 Å, which is also blended; these two lines are not included in the mean. The abundance of A(Nd) = −0.21 from Siqueira-Mello et al. (2013) is compatible within the uncertainties.

4.18 Samarium

The mean of A(Sm) = −0.54 is very close to the value of A(Sm) = −0.51 from Hill et al. (2002).

4.19 Europium

As explained in Section 3.2, the Eu lines require HFS, which we included in our calculations. We obtained a mean of A(Eu) = −0.93 ± 0.07, somewhat lower than A(Eu) = −0.76 from Hill et al. (2002).

4.20 Gadolinium

The 39 measurable Gd lines give a mean of A(Gd) = −0.45 ± 0.10, somewhat lower than A(Gd) = −0.27 from Hill et al. (2002). For the shortest wavelength lines (Gd II 3032.844 and 3034.051 Å), the STIS spectrum is well fitted with A(Gd) = −0.47, and would need a higher Gd abundance by about 0.15 dex to fit the UVES spectrum. The Gd II 3360.712 Å line is blended with NH lines, and Gd II 3482.607 Å is blended with both Co I 3482.634 Å and molecular features, and could not be used.

4.21 Terbium

Most of the 12 Tb lines are well fitted with A(Tb) = −1.26 as derived by Hill et al. (2002), and this applies to the three sets of spectra. The Tb II 3874.168 Å line appears as an asymmetry on the redwards wing of a stronger line. We also inspected the Tb II 2934.802 Å line observed with STIS; this is a weak line, requiring a lower Tb abundance from the order 5 spectrum and a slightly higher value from order 4. Therefore, the higher abundance of A(Tb) = −0.50 derived by Siqueira-Mello et al. (2013) is not justified, and we find a mean value of A(Tb) = −1.22 ± 0.10.

4.22 Dysprosium

Except for the shorter wavelength and weak Dy II 3026.160 Å line measured in the STIS spectrum, the other 27 Dy lines give a mean of A(Dy) = −0.25 ± 0.08, very close to the value of A(Dy) = −0.21 reported by Hill et al. (2002). Therefore, the somewhat higher value of A(Dy) = −0.12 from Siqueira-Mello et al. (2013) is compatible within the uncertainties.

4.23 Holmium

We obtain a mean of A(Ho) = −0.98 ± 0.06. The fits to the four lines are shown in Fig. 5, but the Ho II 3890.925 and 3905.634 Å lines shown in the two lower panels are heavily blended and are not considered in calculation of the final value.

4.24 Erbium

We find a mean of A(Er) = −0.38 ± 0.10, somewhat lower than A(Er) = −0.27 from Hill et al. (2002).

4.25 Thulium

Most of the 10 lines available are well fitted with A(Tm) = −1.24 as derived by Hill et al. (2002). We find a mean of

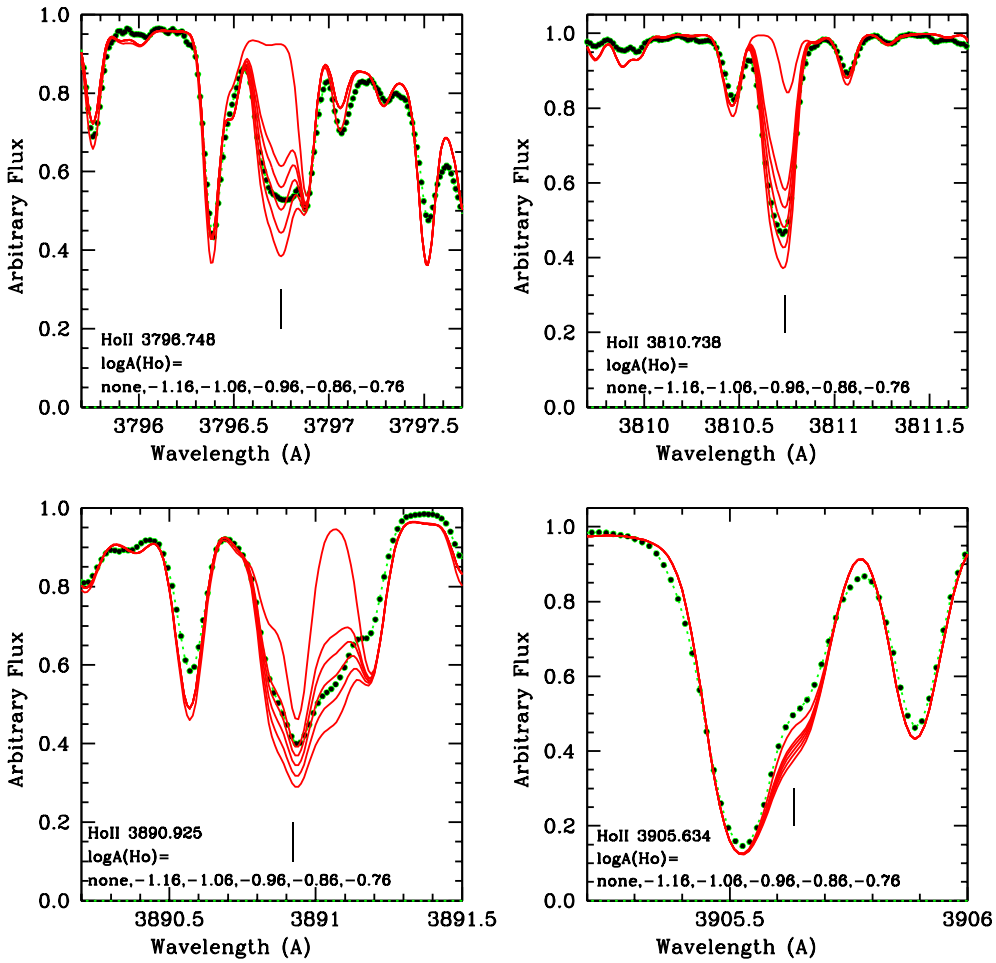

Figure 5. Fits to the Ho II 3796.748, 3810.738, 3890.925, and 3905.634 Å lines in the UVES spectrum (black points), in which the synthetic spectra (red lines) were computed for A(Ho) = none, −1.16, −1.06, −0.96, −0.86, and −0.76.

A(Tm) = −1.32 ± 0.16. The Tm II 3362.615 Å line is blended with NH lines and therefore not reliable as a diagnostic of the Tm abundance.

4.26 Ytterbium

The two lines of Yb are well fitted with A(Yb) = −0.70, somewhat lower than the value of A(Yb) = −0.41 from Sneden et al. (2009); the fits to the lines are shown in Fig. 6. The Yb II 3289.367 Å line is blended with V II 3289.390 Å (χ_{ex} = 1.096 eV, log gf = −0.931) and Fe II 3289.354 Å (χ_{ex} = 3.814 eV, log gf = −1.620). The abundances of Fe and V are well constrained, and therefore these blends do not cause significant uncertainties.

4.27 Lutetium

Lu II 3077.605 Å is effectively the only clear line for lutetium. It is well fitted with A(Lu) = −1.14, or [Lu/Fe] = +1.0. The Lu II 3397.066 Å line is on the redwards wing of another line, and the asymmetry caused by the Lu line is well fitted with A(Lu) = −1.14 as well. Lu II 3472.477 Å is on the bluewards wing of a strong line, and is very weak, and not useful. Finally, Lu II 3554.516 Å line is weak and blended, and shows no sensitivity to the Lu abundance and we do not use it further here.

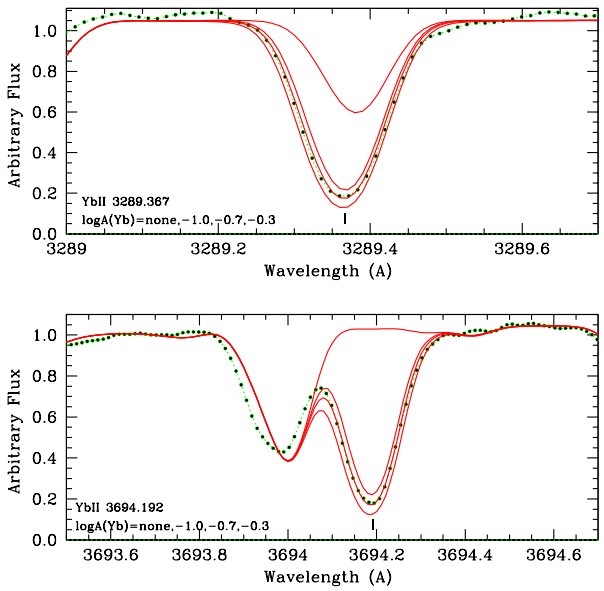

Figure 6. Fits to the Yb II lines in the UVES spectrum (black points), in which the synthetic spectra (red lines) are computed for A(Yb) = none, −1.0, −0.7, and −0.3.

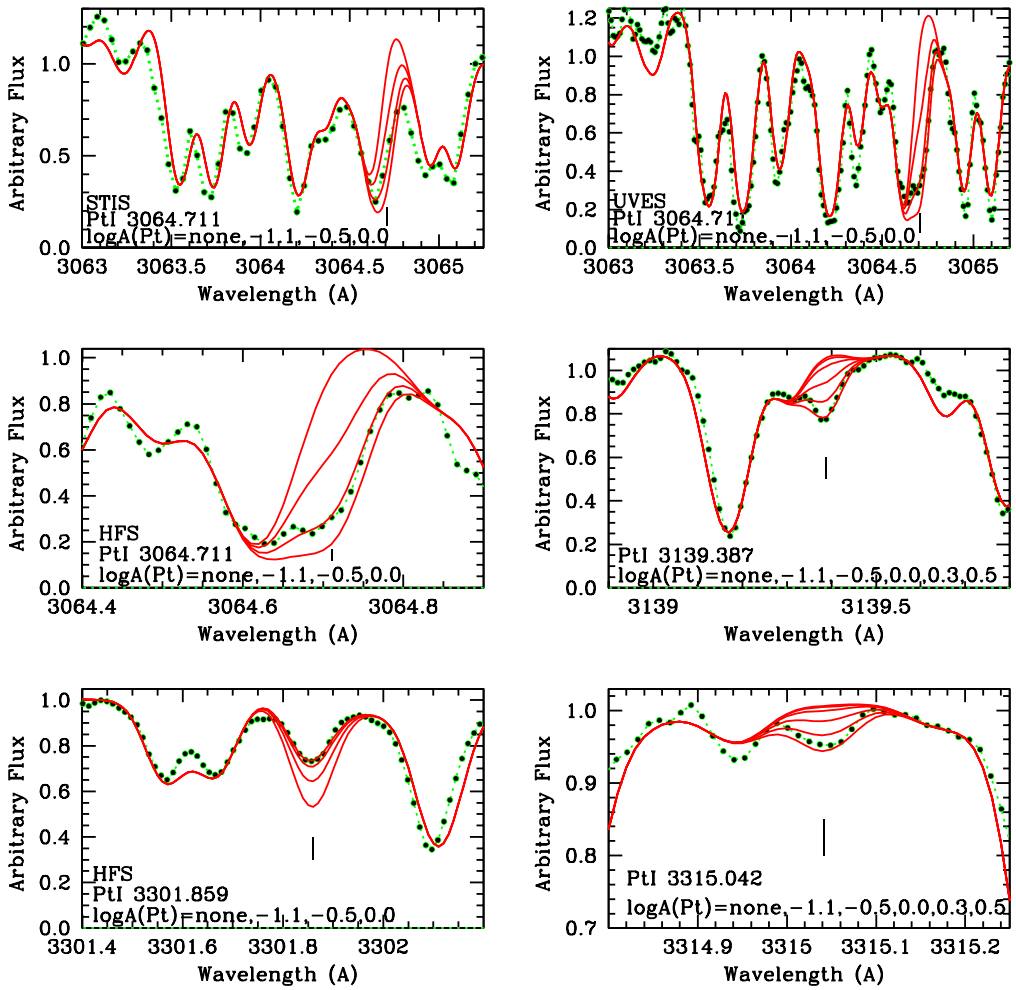

Figure 7. Fits to the Pt I lines. The upper left- and right-hand panels show fits to the 3064.711 Å line in the STIS and UVES data, respectively; the middle left-hand panel shows a zoom-in on the region for the UVES data. The remaining panels show the fits to the other three lines. The synthetic spectra shown (red lines) are computed for A(Pt) = none, −1.1, −0.5, 0.0, +0.3, and +0.5.

4.28 Hafnium

From the seven lines of Hf we obtain a mean of $A(\mathrm{Hf}) = -0.88 \pm 0.05$, somewhat lower than $A(\mathrm{Hf}) = -0.59$ derived by Hill et al. (2002). The Hf II 3793.379 Å line is less reliable than the others because it is in the wing of another stronger line, and many of the nearby lines are not well reproduced.

4.29 Osmium

We have fitted the Os I 3018.036 and 3058.655 Å lines from the STIS order 3 and 2 spectra, respectively. The Os I 3018.036 Å is faint and blended, but can be fitted with $A(\mathrm{Os}) = 0.10$, compatible with $A(\mathrm{Os}) = -0.07$ from Barbuy et al. (2011). The Os I 3058.655 Å line in order 3 of the STIS spectrum appears to be far more reliable, with a higher S/N. We obtain a mean of $A(\mathrm{Os}) = 0.23 \pm 0.16$.

4.30 Iridium

Adopting the abundance $A(\mathrm{Ir}) = +0.20$ from Hill et al. (2002), the Ir I 3047.158 Å line is weak but well fitted, as well as Ir I 3513.648 Å that is located within a set of other lines. We find a mean of $A(\mathrm{Ir}) = 0.10 \pm 0.12$, compatible with $A(\mathrm{Ir}) = 0.20$ from Barbuy et al. (2011) and Hill et al. (2002).

4.31 Platinum

Our fits to the Pt lines are shown in Fig. 7. For the Pt I 3064.711 and 3301.859 Å lines we adopted the HFS splitting from Den Hartog et al. (2005). The Pt I 3064.711 Å line, observed both with UVES and STIS (order 2), is blended with another line, but is clearly seen and gives $A(\mathrm{Pt}) = -0.50$. This is the most reliable indicator, given that it has HFS included, and is not prohibitively blended. The Pt I 3301.859 Å line gives $A(\mathrm{Pt}) = -1.1$, but there is a strong blend and it is not considered further. The Pt I 3139.385 and 3315.042 Å lines have no HFS applied, and give a much higher value of $A(\mathrm{Pt}) = 0.50$. Given the various challenges of the lines we adopt a mean value of $A(\mathrm{Pt}) = 0.00$.

4.32 Gold

The only Au I line available in our spectra (2675.937 Å) is located in STIS order 11. Compared to the study from Barbuy et al. (2011), blending lines on the redward side of the Au I line have now

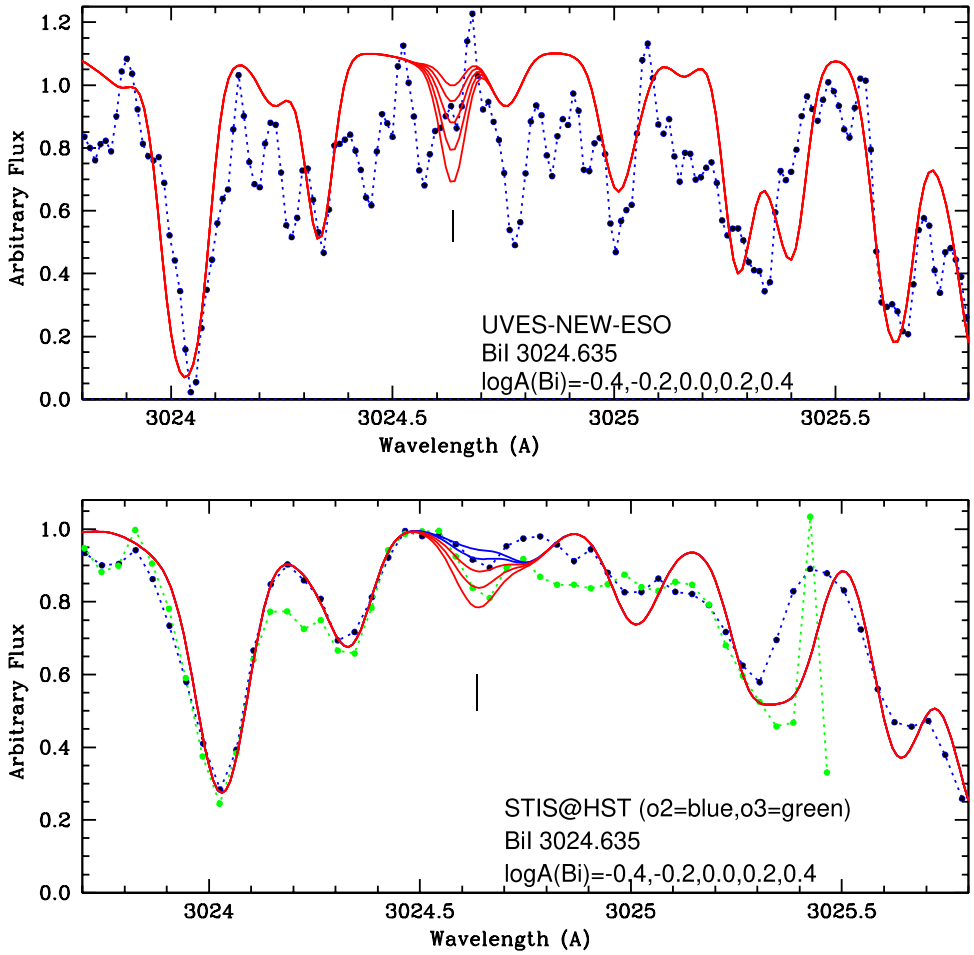

Figure 8. Fits to the Bi I 3024.64 Å line for the UVES and STIS spectra. The UVES spectrum is shown by the blue dotted line in the upper panel, and the STIS order 2 and 3 spectra are shown by the blue and green dotted lines, respectively. The synthetic spectra shown (red lines) are computed for A(Bi) = none, −0.4, −0.2, 0.0, +0.2, and +0.4.

been identified as Fe I 2676.015, 2676.079, and 2676.160 Å, with excitation potentials of 2.728, 2.949, and 2.609 eV, respectively. The oscillator strengths of these lines had to be changed, from −2.404 to −1.35, −0.382 to −1.15, and −1.828 to −1.778, respectively, to fit the feature; the Fe I 2676.015 Å line is particularly important in the blend. A revised value for the Au abundance is now A(Au) = −1.39, or [Au/Fe] = +0.6 adopting $A(\mathrm{Au})_{\odot}$ = 0.91 from Asplund et al. (2021). However, there remains uncertainty due to other blends superimposed on the Au I line, namely, a rather weak line of Fe II 2675.901 Å (χ_{ex} = 5.823 eV, log gf = −2.088), and lines of Co I 2675.981 Å, (χ_{ex} = 0.629 eV, log gf = −1.625), Ta II 2675.900 Å (χ_{ex} = 0.548 eV, log gf = 0.870), and Nb II 2675.939 Å (χ_{ex} = 0.054 eV, log gf = −0.730). The abundances of Co, Nb, and Ta are from Cayrel et al. (2004) and Siqueira-Mello et al. (2013), although the lines of Nb and Ta are weak. Other contaminants reported by Barbuy et al. (2011) are no longer present in the revised line lists from VALD.

4.33 Lead

The two available lines in the 3000–4000 Å region are very faint and cannot be used: Pb I 3639.568 Å is not detectable, and Pb I 3683.462 Å is detectable but weak and in the wing of a very strong line, and therefore not measurable. The Pb I 2833.053 Å line in the STIS spectrum (with a nearby Ir II 2833.241 Å line) has an excitation potential of 1.453 eV and the oscillator strength from VALD of log gf = 1.924 had to be corrected to −0.30 to fit the line. This UV Pb I line is well fitted with A(Pb) = −0.65, in agreement with Barbuy et al. (2011), and only 0.1 dex lower than the value of A(Pb) = −0.55 given by Plez et al. (2004) from Pb I 4057.8 Å.

4.34 Bismuth

The Bi I 3024.635 Å line was observed both with UVES and with STIS (in orders 2 and 3), and the fits are shown in Fig. 8. In our fits we tried to adopt log gf = −0.15 as reported in NIST and measured by Wahlgren et al. (2001). This value contrasts with the log gf = 1.35 adopted by Barbuy et al. (2011), from measurements by Andersen et al. (1972) and which had been adopted by VALD and included in the Kurucz line lists. However, the smaller value leads to A(Bi) = 1.5 and [Bi/Fe] = +3.75 that is far too overenhanced and probably not realistic, and we therefore retained the previous log gf = 1.35 in our calculations. Our fit to the order 2 STIS spectrum (blue line in the figure) gave A(Bi) = −0.2, and is more reliable than the fit to order 3, which give A(Bi) = +0.2 (green line). In the higher resolution UVES spectrum (upper panel), despite the noise, it appears to be compatible

with A(Bi) = −0.2. As pointed out by Barbuy et al. (2011), the Bi abundance is an important calibration point for zero-age r-process abundance distribution models (Schatz et al. 2002).

4.35 Thorium

Six lines are weak but measurable and give a mean of A(Th) = −1.04 ± 0.08, very close to the value of A(Th) = −0.98 from Hill et al. (2002). The Th II 3180.194 Å line is not only weak but also blended with a strong line, and the overall feature is very insensitive to the Th abundance. We also note that the Th II 3675.567 Å line is well fitted, but that the surrounding lines are not well reproduced with the present line list, even if this does not affect the Th line.

4.36 Uranium

Cayrel et al. (2001) derived A(U) = −1.6, and Hill et al. (2002) revised the value to A(U) = −1.92, as a result of a new measurement of the line oscillator strength from the UVES spectra. Barbuy et al. (2011) adopted this latter value, which we also adopt here.

4.37 Uncertainties

The final abundances in Table 2 correspond to the estimates from the UVES raw (non-smoothed) spectra. We consider this as the best quality spectrum, taking into account the excellent sampling of these data, with a pixel scale of 0.0147 Å pixel^{-1} and ≥5 pixels per resolution element. Table 3 gives the uncertainties from (a) the fits to lines in the STIS spectra for wavelengths <3070 Å, and otherwise the smoothed UVES spectrum centred at 3400 Å; (b) fits to the Keck spectra; and (c) fits to the raw (non-smoothed) UVES spectrum.

The statistical uncertainty was computed through the standard deviation formula,

$$\sigma = \sum_{i=1}^{N} \sqrt{\frac{(X_i - \mu)^2}{N}},$$

and added to this are the systematic uncertainties resulting from stellar parameters (column 3 of Table 3). For most of the elements we adopted the errors in stellar parameters as given in table 6 of Hill et al. (2002), and also took into account the errors computed by Siqueira-Mello et al. (2013) and Sneden et al. (2009). For the remaining elements that had not been analysed before we estimated the error by computing models with $\Delta T = +100$ K, $\Delta \log g = +0.3$ dex, and $\Delta v_t = +0.2$ km s^{-1}. Table 4 reports the uncertainties for elements not studied previously.

The mean final abundances in Table 2 were obtained from the mean value among the spectral lines considered in Table A1, in some cases excluding the outliers. For some elements the previous abundance estimates from the STIS spectra were kept as the final value as the quality of the observed lines is better for some lines in these data.

5 DISCUSSION

The presence of heavy elements in very old metal-poor halo stars should be due to a source of r-process elements in the early Galaxy, as suggested by Truran (1981), given that there might not be enough time for AGB stars to form these elements in an s-process. On the other hand, Frischknecht, Hirschi & Thielemann (2012), Frischknecht et al. (2016), and Limongi & Chieffi (2018) demonstrated that metal-poor rotating massive stars are able to synthesize neutron-capture elements through an s-process.

Table 3. Abundances for CS 31082−001 and their uncertainties from analysis of: (a) STIS spectra plus UVES smoothed spectra (tagged as SU), (b) Keck-HIRES spectra (tagged as Keck), and (c) non-convolved UVES spectra (tagged as UVES). The stellar parameter uncertainty ($\sigma_{\rm param}$) was adopted from Hill et al. (2002), Sneden et al. (2009), and Siqueira-Mello et al. (2013), except for those with uncertainties presented in Table 4 (Ge, Mo, Sn, Ho, Yb, Lu, Hf, Pt, and Bi). The statistical (fitting) uncertainties in columns 6, 8, and 10 are internal errors, or in the case of a unique line is an estimation of the fitting error.

Element	Z	$\sigma_{\rm param}$	N	A(X)$_{\rm SU}$	$\sigma_{\rm SU}$	A(X)$_{\rm Keck}$	$\sigma_{\rm Keck}$	A(X)$_{\rm UVES}$	$\sigma_{\rm UVES}$
Ge	32	0.150	1	0.48	0.05	...	...	0.48	...
Sr	38	0.092	2	0.40	0.02	0.35	0.00	0.40	0.00
Y	39	0.121	22	−0.21	0.06	−0.48	0.14	−0.37	0.17
Zr	40	0.114	66	0.36	0.10	0.27	0.14	0.26	0.15
Nb	41	0.128	3	−0.55	0.00	−0.70	0.05	−0.72	0.05
Mo	42	0.070	1	−0.11	...	−0.24	...	−0.21	0.05
Ru	44	0.159	5	0.27	0.04	0.18	0.02	0.18	0.02
Rh	45	0.162	3	−0.42	0.00	−0.49	0.04	−0.51	0.09
Pd	46	0.166	5	−0.10	0.06	−0.17	0.10	−0.21	0.07
Ag	47	0.166	2	−0.96	0.05	−0.94	0.02	−0.94	0.07
Sn	50	0.200	1	−0.90	...	...	...	<−0.40	0.10
Ba	56	0.122	1	0.15	...	0.00	...	−0.05	0.02
La	57	0.128	6	−0.65	0.08	−0.72	0.11	−0.73	0.07
Ce	58	0.119	18	−0.31	0.00	−0.40	0.09	−0.41	0.11
Pr	59	0.119	3	−0.86	0.00	−0.94	0.02	−0.94	0.02
Nd	60	0.119	24	−0.13	0.00	−0.34	0.10	−0.33	0.09
Sm	62	0.122	26	−0.48	0.12	−0.56	0.17	−0.54	0.18
Eu	63	0.120	6	−0.78	0.04	−0.96	0.10	−0.93	0.07
Gd	64	0.120	39	−0.28	0.09	−0.44	0.13	−0.45	0.10
Tb	65	0.121	11	−1.26	0.00	−1.23	0.09	−1.22	0.08
Dy	66	0.118	28	−0.22	0.05	−0.28	0.09	−0.25	0.08
Ho	67	0.140	3	−0.97	0.05	−0.98	0.06	−0.98	0.06
Er	68	0.142	21	−0.29	0.04	−0.39	0.09	−0.38	0.10
Tm	69	0.115	10	−1.22	0.12	−1.25	0.16	−1.32	0.16
Yb	70	0.210	2	−0.70	0.02	−0.62	0.22	−0.67	0.00
Lu	71	0.060	2	−1.14	0.00	−0.94	0.00	−1.14	0.05
Hf	72	0.070	6	−0.64	0.11	−0.85	0.06	−0.88	0.05
Os	76	0.157	3	0.20	0.07	0.18	0.08	0.23	0.16
Ir	77	0.140	5	0.22	0.16	0.20	0.14	0.10	0.12
Pt	78	0.040	4	−0.80	0.30	−1.10	0.00	−0.80	0.30
Bi	83	0.200	1	−0.20	0.00	...	...	...	...
Th	90	0.132	6	−0.98	0.00	−0.96	0.09	−1.04	0.08

Table 4. Abundance uncertainties from stellar parameters for CS 31082−001 for uncertainties of $\Delta T_{\rm eff} = 100$ K, $\Delta \log g = 0.3$, $\Delta v_t = 0.2$ km s^{-1} for the elements not studied by Hill et al. (2002).

Element	$\Delta T_{\rm eff}$ 100 K	$\Delta \log g$ 0.3 dex	Δv_t 0.2 km s^{-1}	$(\sum x^2)^{1/2}$
(1)	(2)	(3)	(4)	(5)
[Ge/Fe]	+0.15	+0.03	+0.00	0.15
[Mo/Fe]	+0.01	+0.06	+0.03	0.07
[Sn/Fe]	+0.20	+0.00	+0.00	0.20
[Ho/Fe]	+0.02	±0.10	±0.10	0.14
[Yb/Fe]	+0.06	+0.03	−0.20	0.21
[Lu/Fe]	+0.01	+0.06	+0.00	0.06
[Hf/Fe]	+0.03	+0.06	+0.00	0.07
[Pt/Fe]	+0.03	−0.03	+0.00	0.04
[Bi/Fe]	+0.20	−0.02	+0.00	0.20

Sneden, Cowan & Gallino (2008, and references therein) reviewed the formation of heavy elements through the s- and r-process and showed that the abundance pattern of the heaviest r-process elements, i.e. those with atomic number 56 < Z < 78, is the same in different objects, including the Sun. The same does not apply to the trans-iron elements (31 < Z < 52) and the actinides (89 < Z < 92).

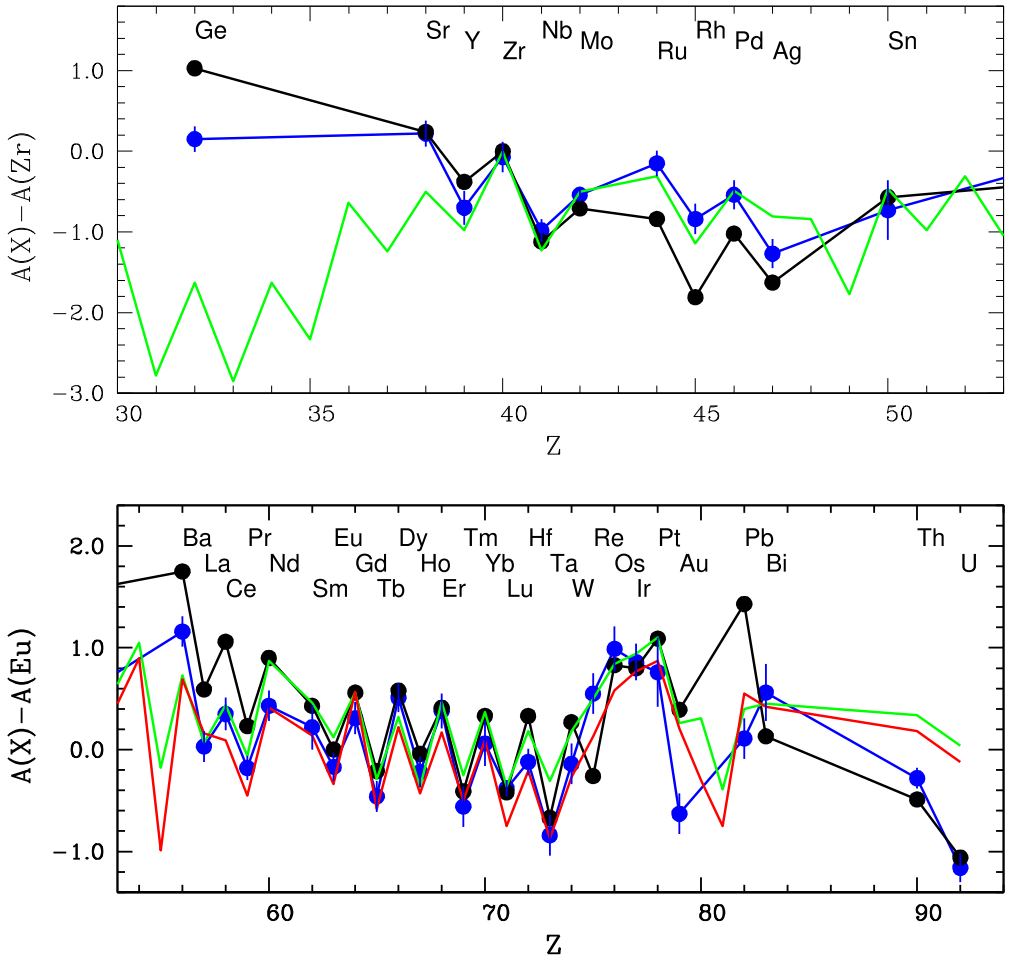

Figure 9. Abundance patterns of CS 31082−001 (blue) and the Sun (black) compared with models for a neutrino wind scenario for a hot r-process (red, from Wanajo et al. 2002) and for a cold r-process (green, from Wanajo, 2007). Upper panel: lower neutron-capture elements from Ge ($Z = 32$) to Sn ($Z = 50$), normalized to the abundance of Zr. Lower panel: heavier neutron-capture elements from Ba ($Z = 56$) to U ($Z = 92$), normalized to the abundance of Eu. We have assumed uncertainties of ±0.20 for Ta, W, Re, Au, and Pb.

In general terms, the production of the lightest neutron-capture elements (that appear to vary from star to star) has been assigned to a Light Element Primary Process (LEPP; Travaglio et al. 2004), an i-process (Cowan & Rose 1977; Roederer et al. 2016), neutrino-driven winds in supernovae (Arcones & Montes 2011, and references therein), or a weak r-process (Wanajo 2013); see further discussion by Spite et al. (2018) and Peterson, Barbuy & Spite (2020).

The r-process was more recently reviewed by Cowan et al. (2021). Traces of r-process element production were confirmed from the neutron star merger (NSM) kilonova AT2017gfo that was associated with the gravitational-wave event GW170817 (Drout et al. 2017; Tanvir et al. 2017). Other likely sources are mergers of neutron stars with a black hole, magnetorotational supernovae (Winteler et al. 2012), and collapsars (Siegel, Barnes & Metzger 2019).

The nucleosynthesis of neutron-capture elements in massive stars has been explored by several studies, including Wanajo (2007), Just et al. (2015), Banerjee, Qian & Heger (2018), and Ritter et al. (2018). Here we compare the r-process abundances for CS 31082−001 with calculations from Wanajo (2007) and Just et al. (2015).

For background, the neutrino winds that arise in core-collapse supernovae are expected to produce all of the r-process elements until the actinides. Wanajo et al. (2002) computed a model with a compact neutron star of 2.0 $M_\odot$, and a neutrino sphere of 10 km. They established a freeze-out temperature, specified as the final temperature of the neutrino winds, to be $T_{9f} = 1.0$ (in units of 10^9 K), to better reproduce the solar r-process pattern near the third peak. Wanajo (2007) adopted $T_{9f} = 0.1$ instead, which he called the cold r-process, in which the neutron capture competes with the β-decay, similar to the hot r-process. The cold r-process also predicts a low lead production that is compatible with its estimated abundance in CS 31082−001.

In Fig. 9, we show the abundance pattern of CS 31082−001 compared with the solar pattern (Asplund et al. 2021), and the models of a neutrino wind scenario for a hot r-process (Wanajo et al. 2002) and for a cold r-process (Wanajo, 2007). The lighter neutron-capture elements are normalized to the Zr abundance, and the heavier elements are normalized to the Eu abundance (see discussion below).

Wanajo et al. (2014) proposed the first yield calculations of a NSM, based on full general relativistic, approximate neutrino transport simulations for masses of 1.3–1.35 $M_\odot$. These appeared as a promising candidate for r-process enrichment in the Galaxy, given that the ejecta consist of almost pure neutrons. Models from Just et al. (2015) also included the black hole torus ejecta, formed after the NSM.

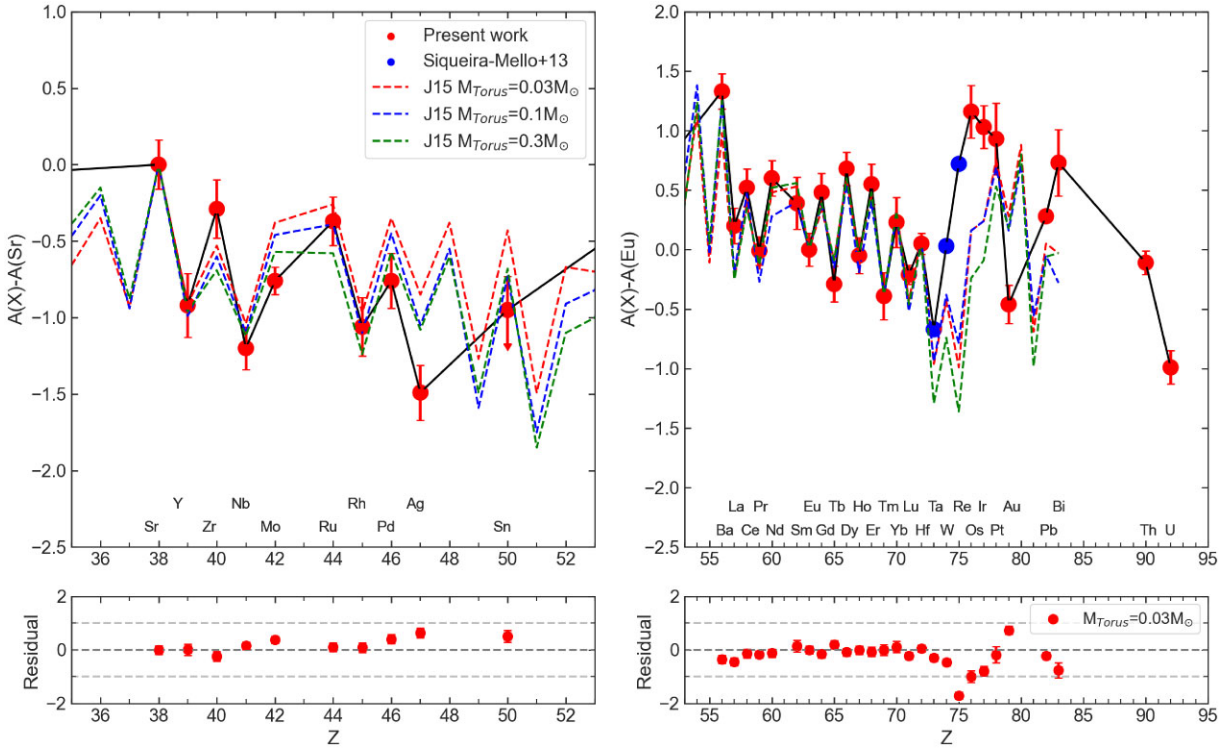

Figure 10. Abundance pattern of CS 31082−001 (red and blue dots linked by the black line) compared with models from Just et al. (2015) for black hole torus masses of 0.03, 0.1, and 0.3 $M_\odot$. Left: abundances are normalized to Sr showing the elements from Sr to Sn. Right: elements from Ba to U with abundances normalized to Eu. The lower panels show the residuals between the model with $M_{\rm Torus} = 0.03$ $M_\odot$ and the abundance pattern of CS 31082−001.

In Fig. 10, the abundances of CS 31082−001 are compared with the models from Just et al. (2015) for torus masses of 0.03, 0.1, and 0.3 $M_\odot$. We see a general agreement, with Zr enhanced, Pd–Sn deficient, and Hf–Pt enhanced. At least for the abundance pattern, there is reasonable agreement with the NSM models.

Adopting the nucleosynthesis predictions from Wanajo et al. (2014) and Just et al. (2015), Kobayashi et al. (2023) revised the r-process enrichment, intending to investigate if NSMs could be the main contributor to r-process elements in the Galaxy. Their models adopting magnetorotational supernovae (adopting the calculations from Nishimura et al. 2015) best reproduce the observations, so they concluded that NSMs are probably not the main contributor to r-process elements. Alongside this, we note that Holmbeck et al. (2019) found that the production of actinides is probably due to NSMs, and that they also concluded that another source was required to account for the observed r-process abundances.

5.1 Trans-iron elements: Ge, Sr, Y, Zr, Nb, Mo, Ru, Rh, Pd, Ag, Sn

The so-called trans-iron elements, with atomic numbers $31 < Z < 52$, include elements from Ga ($Z = 31$) to Te ($Z = 52$).

Germanium can be considered the last of the upper iron-peak group or the first of the neutron-capture elements (Woosley & Weaver 1995), or both at the same time (Niu et al. 2014). To further understand the origin of Ge, Cowan et al. (2005) and Siqueira-Mello et al. (2013) compared its abundance in metal-poor stars with that of the r-process element Eu. They showed that the Ge abundance correlates with metallicity, but not with Eu, suggesting that Ge is not a typical r-process element.

As discussed above, and pointed out by Kratz et al. (2007), the trans-iron element abundances vary from star to star and require an additional secondary weak r-process site (Spite et al. 2018; Peterson et al. 2020). Roederer et al. (2022a,b) instead suggested that the universality of the r-process accepted in the literature for the $56 < Z < 71$ from Ba to Lu, and the third peak r-process elements with $72 < Z < 78$ from Hf to Pt, might also apply to first peak s-elements, or light s-elements (ls) Se, Sr, Y, Zr, and Mo, provided that these are scaled independently from the other elements.

From Fig. 9 it appears that, for the lighter neutron-capture elements, the abundance pattern of the trans-iron elements Sr to Mo is rather similar to solar, and Mo to Ag are enhanced, whereas Sn is deficient in CS 31082−001. This is in agreement with the suggestion from Roederer et al. (2022a,b) that the Sr to Mo abundance pattern is universal, whereas from Ru through to Sn it does not appear so. The hot and cold r-process models from Wanajo (2007) coincide in this element number range ($38 < Z < 42$), and fit the abundances of CS 31082−001 well (as previously discussed by Barbuy et al. 2011; Siqueira-Mello et al. 2013).

5.2 Second peak elements: Ba, La, Ce, Pr, Nd

Ba, La, Ce, Pr, and Nd correspond to second peak s-elements or heavy-s (hs). These elements are dominantly s-process elements in stars like the Sun, but in CS 31082−001 their production is likely due to an early r-process. They show a mean enhancement of [(Ba, La, Ce)/Fe] = +1.0 and [(Pr, Nd)/Fe] = +1.18 (see Table 5).

These elements are well fitted by the hot and cold models from Wanajo (2007), but they are deficient relative to the solar abundance pattern (Fig. 9).

Table 5. r- and s-process contributions from Simmerer et al. (2004) and Prantzos et al. (2020) for solar composition and abundance enhancements of different groups of elements. The fractions by Prantzos et al. (2020) that do not add to 100 per cent are due to a contribution from the p-process. ':' means uncertain.

Element	Z	r-fraction	s-fraction	$A(X)_{adopted}$	$[X/Fe]_{adopted}$	$[X/Fe]_{Mean}$
Ge	32	0.431/0.364	0.569/0.636	0.48	−0.24	−0.24
Sr	38	0.11/0.083	0.89/0.912	0.55	0.62	
Y	39	0.281/0.222	0.719/0.778	−0.37	0.32	+0.50
Zr	40	0.191/0.183	0.809/0.817	0.26	0.57	
Nb	41	0.324/0.349	0.676/0.651	−0.65	0.78	+0.80
Mo	42	0.323/0.275	0.677/0.497	−0.21	0.81	
Ru	44	0.61/0.591	0.39/0.338	0.18	1.33	
Rh	45	0.839/0.878	0.161/0.122	−0.51	1.61	+1.27
Pd	46	0.555/0.542	0.445/0.448	−0.21	1.12	
Ag	47	0.788/0.791	0.212/0.209	−0.94	1.00	
Sn	50	0.225/0.301	0.775/0.680	−0.40	0.48	+0.48
Ba	56	0.147/0.109	0.853/0.888	0.40	1.03	
La	57	0.246/0.200	0.754/0.799	−0.73	1.06	+1.00
Ce	58	0.186/0.148	0.814/0.848	−0.41	0.91	
Pr	59	0.508/0.465	0.492/0.535	−0.94	1.21	+1.18
Nd	60	0.421/0.385	0.579/0.615	−0.133	1.15	
Sm	62	0.669/0.647	0.331/0.325	−0.54	1.41	
Eu	63	0.973/0.951	0.027/0.049	−0.93	1.45	
Gd	64	0.819/0.835	0.181/0.163	−0.45	1.37	
Tb	65	0.933/0.928	0.067/0.072	−1.22	1.37	
Dy	66	0.879/0.847	0.121/0.151	−0.25	1.55	+1.45
Ho	67	0.936/0.926	0.064/0.074	−0.88	1.44	
Er	68	0.832/0.799	0.168/0.184	−0.38	1.59	
Tm	69	0.829/0.872	0.171/0.128	−1.32	1.47	
Yb	70	0.682/0.570	0.318/0.429	−0.70	1.35	
Lu	71	0.796/0.796	0.204/0.204	−1.14	1.66	
Hf	72	0.51/0.393	0.49/0.605	−0.88	1.17	
Ta	73	0.588/0.497	0.412/0.503	−1.60	1.45	+1.28
W	74	0.462/0.397	0.538/0.601	−0.90	1.21	
Re	75	0.911/0.846	0.089/0.154	−0.21	2.41	+2.41
Os	76	0.916/0.897	0.084/0.103	0.23	1.78	
Ir	77	0.988/0.989	0.012/0.011	0.10	1.68	+1.73
Pt	78	0.949/0.922	0.051/0.078	0.00	1.29	+1.29:
Au	79	0.944/0.942	0.056/0.058	−1.39	0.60	+0.45
Pb	82	0.214/0.169	0.786/0.831	−0.65	0.30	
Bi	83	0.647/0.784	0.353/0.216	−0.20	2.05	+2.05
Th	90	1.00/1.00	0.00/0.00	−1.04	1.83	+1.68
U	92	1.00/1.00	0.00/0.00	−1.92	1.52	

5.3 Very enhanced r-process elements: Sm, Eu, Gd, Tb, Dy, Ho, Er, Tm, Yb, Lu, Hf, Os, Ir, Pt, Au

The elements discussed in this section are dominantly r-process elements in the Sun, and they are strongly enhanced in CS 31082−001.

The elements from Sm ($Z = 62$) to Lu ($Z = 71$) show a mean r-process enhancement of [r-elements/Fe] = +1.45. These include the first estimates for Ho and Yb from these data, which are close to the mean with [Ho/Fe] = +1.44 and [Yb/Fe] = +1.35 (see Table 5). Os ($Z = 76$) and Ir ($Z = 77$) also show a mean r-process enhancement of [r-elements/Fe] = +1.73, and the actinides Th ($Z = 90$) and U ($Z = 92$) show [r-elements/Fe] = +1.68.

Hf ($Z = 72$) is produced as an r- and s-element in proportions of 0.51 and 0.49, respectively, in the solar mixture (Simmerer et al. 2004,) and can potentially discriminate the site production of r-process elements (Eichler, Sayar & Arcones 2019). The Hf/Eu and Hf/Th ratios show the balance between the NSMs that mostly produce Hf and the Type II supernovae responsible for Eu and Th. The $\log \epsilon(\mathrm{Th/Hf}) = A(\mathrm{Th}) - A(\mathrm{Hf}) = -0.16$ in CS 31082−001 is compatible with the r-process production from Eichler et al. (2019; lower left-hand panel of their fig. 2). The same conclusion is reached

from the value of A(Hf) − A(Eu) = +0.05 in CS 31082−001 that corresponds to a pure r-process enrichment of Hf (see Roederer et al. 2009, upper left-hand panel of their fig. 6).

The estimate for Au (Z = 79) from one STIS line, revised with respect to Barbuy et al. (2011), results in a lower enhancement of [Au/Fe] = +0.60; in principle, Au is almost entirely due to the r-process.

The heavier neutron-capture r-process elements are well fitted by the solar abundance pattern and by the hot and cold models from Wanajo (2007), as shown in Fig. 9. This pattern can be considered as universal as explained by Roederer et al. (2022a,b and references therein).

5.4 Heaviest stable elements: Pb, Bi

Pb and Bi could be considered as a third peak of the s-elements (Sneden et al. 2008), or early production as an r-product, as discussed by Plez et al. (2004). Cowan et al. (1999) reported that calculations reproduce the solar isotopic r-abundances, including the heaviest stable Pb and Bi isotopes, at the same time that about 85 per cent of Pb and Bi are formed through the radioactive decay of Th and U.

The solar isotopic fractions from Asplund et al. (2009) were 1.997, 18.582, 20.563, and 58.858 for ^{204}Pb, ^{206}Pb, ^{207}Pb, and ^{208}Pb, respectively. Plez et al. (2004) investigated what would be the minimum amount of lead due to the decay of ^{238}U and ^{232}Th into ^{206}Pb and ^{208}Pb, respectively, for the Sun. They then also estimated this for CS 31082−001 by adopting an age of 13.5 ± 1.5 Gyr and decay times of τ = 4.47 and 14.05 Gyr for ^{238}U and ^{232}Th, respectively. The conversion ^{235}U into ^{207}Pb was also computed but using theoretical values. The resulting lead abundance of −0.61 < A(Pb) < −0.55 was very close to the observed Pb abundance, with the conclusion that effectively all of the Pb was a result of the decay of ^{238}U, ^{232}Th, and ^{235}U.

As discussed by Plez et al. (2004) and Barbuy et al. (2011), nucleosynthesis calculations predict that the total Pb abundance is the sum of any assumed initial r-process Pb production, plus the radioactive decay products of Th and U, and suggest a higher Pb abundance for CS 31082−001 than observed. According to Roederer et al. (2009), stars with A(La) − A(Eu) > +0.25 show some amount of s-process material, whereas those with +0.09 < A(La) − A(Eu) < +0.23 show a pure r-process content. In CS 31082−001 this quantity gives A(La) − A(Eu) = +0.20, typical of r-process nucleosynthesis. Therefore, it should not show any s-process contribution to Pb, and its value of A(Pb) − A(La) = +0.08 is compatible, and even lower, than that from a pure r-process (Roederer et al. 2009, see lower panel of their fig. 5).

For Bi, the s-process terminates at ^{209}Bi, the last stable isotope, which is actually radioactive but with a half-life longer than a Hubble time. Its abundance in CS 31082−001 is compatible with r-process production (Fig. 9) but appears enhanced relative to the predictions from Just et al. (2015, see Fig. 10). The result of [Bi/Fe] = +2.05 shows an r-process enhancement comparable to the other elements studied here. However, if we adopt the oscillator strength indicated in NIST of log gf = −0.15, instead of the log gf = 1.35 previously available and adopted here, we would have [Bi/Fe] = +3.75, which is unexpectedly high. It is difficult to understand why Bi would show an s-process contribution in this star, while Pb does not, but it is also difficult to accept that this element is much more enriched in some r-process nucleosynthesis than any of the other elements. Even if s-process heavy-element production by spinstars is included, Bi is enhanced but not more than the other studied elements (Frischknecht et al. 2016).

In short, results for both Pb and Bi are intriguing and remain open for further studies.

5.5 Actinides: Th, U

The Th and U abundances for CS 31082−001 were discussed extensively by Cayrel et al. (2001) and Hill et al. (2002), and its age by Barbuy et al. (2011), so we do not revisit these points here. Th and U are entirely r-process element, and their enhancements of [Th/Fe] = +1.83 and [U/Fe] = +1.52 indicate they are produced in the same process as the other r-process elements.

To summarize this section, following the proportion of r- to s-process contributions presented by Simmerer et al. (2004) and Prantzos et al. (2020) for the solar mixture, the mean abundance enhancements from the r-process- or s-process-dominated elements for different groups are given in Table 5. It is clear that the r-process-dominated elements are more enhanced than others, as seen in Fig. 11. This figure also compares the r-process abundance pattern of CS 31082−001 to that of the Sun that we obtained by multiplying each element abundance adopted in the star with the solar r-fraction from Prantzos et al. (2020), normalized to the abundance of Au; this pattern again shows the r-process nature of the neutron-capture elements in CS 31082−001.

6 CONCLUSIONS

The halo star CS 31082−001 is among the most completely analysed in terms of elemental abundances, with estimates for 60 elements. Past results were available for 54 elements from Hill et al. (2002), Plez et al. (2004), Barbuy et al. (2011), and Siqueira-Mello et al. (2013), which we have supplemented with abundances for Be, V, and Cu from E22, and now Sn, Ho, and Yb in this study. The only star with a greater number of elemental abundances is HD 222925, with estimates for 63 elements (Roederer et al. 2022b). However, with [Fe/H] = −1.4, the metallicity of HD 222925 is very different to that of CS 31082−001. This means that HD 222925 was probably enriched later, and included s-process contributions from AGB stars, whereas the heavy-element abundances in CS 31082−001 are all due to the r-process (except for the possibility of s-process elements from spinstars).

We now briefly summarize our main conclusions.

(i) As a general conclusion, we confirm the r-process-dominated elements are very enhanced and compatible with the r-process pattern of the Sun (Table 5 and Fig. 11).

(ii) Ge is deficient relative to the solar abundance pattern, indicating that Ge is dominantly an iron-peak element and not a neutron-capture element (except perhaps for a small fraction).

(iii) Ho is enhanced by [Ho/Fe] = +1.44, which is compatible with the enhancements of Gd, Tb, Dy, Tm, and Lu, although somewhat lower than those of a few other elements. Roederer et al. (2022b) pointed out that for HD 222925, the Ho abundance is the most discrepant relative to the solar pattern, but this is not the case for CS 31082−001.

(iv) Our estimate for Yb is compatible with the other r-element enhancements in CS 31082−001.

(v) With [Sn/Fe] = 0.48, the enhancement of Sn is compatible with that of trans-iron elements Mo and Ag, but is lower than seen for others (e.g. Ru, Rh, and Pd). The first Sn detection in an r-process-rich star was for HD 222925 from Roederer et al. (2022b). Our estimate for CS 31082−001 is therefore the second, albeit only an upper limit.

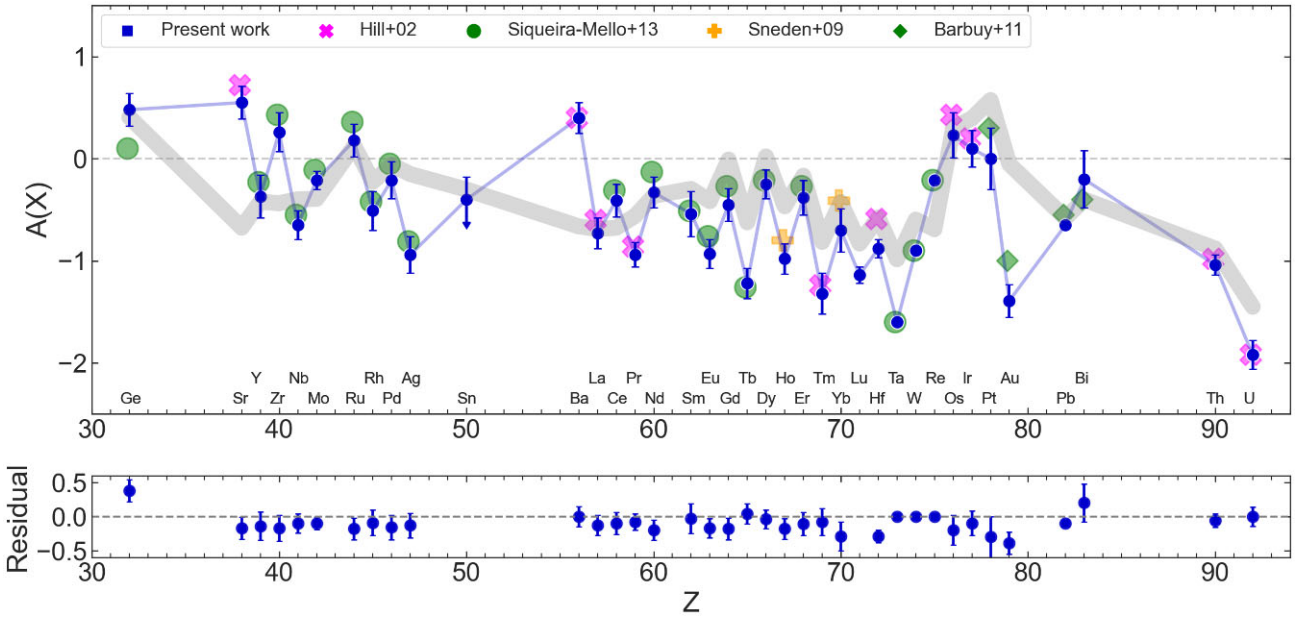

Figure 11. Abundance pattern of CS 31082−001 comparing the non-normalized abundances obtained in this work using the near-UV lines with those from the visible (Hill et al., 2002) and UV regions (Sneden et al., 2009; Barbuy et al. 2011; Siqueira-Mello et al. 2013). The residuals are shown in the lower panel from the abundance comparison between this work and the literature. The shaded grey line is the solar pattern corresponding to the element abundance multiplied by its r-fraction normalized to the abundance of Au.

(vi) Elements in the range $31 \leq Z \leq 50$, i.e. from Ge to Sn, do not scale with the solar abundance pattern (see upper panel of Fig. 9), thus agreeing with the conclusion of Roederer et al. (2022b).

(vii) Elements with $Z \geq 56$ (i.e. Ba and heavier) match the solar abundance pattern (see lower panel of Fig. 9), as suggested previously by Cowan et al. (1999) and Roederer et al. (2010, 2022b and references therein).

(viii) The heavier elements Pt, Au, Pb, and Bi are intriguing. The Pt abundance is very uncertain, and could be lower if the line computed with HFS was considered. The [Au/Fe] and [Pb/Fe] abundances appear too low relative to all other elements. For Bi we have conservatively adopted the oscillator strength of 1.35 previously available, but a value of −0.15 is now indicated in NIST, which would give a very high [Bi/Fe] = 3.75, rather than the [Bi/Fe] = 2.05 as adopted. Bi is the most intriguing element of all, and has not been well studied in the literature. Further studies of these elements in r-process-rich metal-poor stars should be pursued.

Finally, the characterization of the whole abundance pattern for an r-II star ([Eu/Fe] $>$ +0.7, cf. Holmbeck et al. (2020), and [Ba/Eu] $<$ 0.0) can be a key aspect in determining not only the nucleosynthesis channels that create every element in the early stages of the Galaxy, but also the origin of these stars. Roederer et al. (2018) analysed the orbital parameters for r-II stars, including CS 31082−001, and suggested that stars with [Eu/Fe] $>$ +0.7 are only found in halo-like orbits and were probably formed in a low star formation efficiency environment similar to those found in dwarf galaxies. This finding is also supported by the cosmological zoom-in simulations by Hirai et al. (2022), where the r-II stars are predominantly formed ∼10 Gyr ago within low-mass dwarf galaxies that were later disrupted. The time-scale for the r-II stars from Hirai et al. (2022) is compatible with the age of 14.0 ± 2.4 Gyr derived for CS 31082−001 by Hill et al. (2002) and Barbuy et al. (2011). Looking ahead, further study of the origins of the few known actinide-rich stars will be important to understand their physical properties and chemical-enrichment histories.

ACKNOWLEDGEMENTS

HE acknowledges a CAPES PhD fellowship and a project grant from the Knut and Alice Wallenberg Foundation (KAW 2020.0061 Galactic Time Machine). MJC acknowledges a previous IC FAPESP fellowship 2020/14944-4 and a CNPq Master fellowship. BB acknowledges grants from FAPESP, CNPq, and CAPES – Financial code 001.

This study is based on observations made with the ESO Very Large Telescope at Paranal Observatory, Chile: Program ID: 165.N-0276 (PI: R. Cayrel). This research is also based on observations made with the NASA/ESA *Hubble Space Telescope* obtained from the Space Telescope Science Institute, which is operated by the Association of Universities for Research in Astronomy, Inc., under NASA contract NAS 5-26555. These observations are associated with program 9359 (PI: R. Cayrel). Some of the data presented herein were obtained at the W. M. Keck Observatory, which is operated as a scientific partnership among the California Institute of Technology, the University of California, and the National Aeronautics and Space Administration. The Observatory was made possible by the generous financial support of the W. M. Keck Foundation. The Keck observations are related to program U53H (PI: M. Bolte).

DATA AVAILABILITY

Observed data are available at the ESO and *HST* archives. Reduced data and calculated synthetic spectra available under request.

REFERENCES

Abbott B. P. et al., 2017, ApJ, 851, L35
Alvarez R., Plez B., 1998, A&A, 330, 1109

Andersen T., Madsen O. H., Sorensen G., 1972, J. Opt. Soc. Am., 62, 1118
Arcones A., Montes F., 2011, ApJ, 731, 5
Asplund M., Amarsi A. M., Grevesse N., 2021, A&A, 653, A141
Asplund M., Grevesse N., Sauval A. J., Scott P., 2009, ARA&A, 47, 481
Banerjee P., Qian Y.-Z., Heger A., 2018, ApJ, 865, 120
Barbuy B. et al., 2011, A&A, 534, A60
Beers T. C., Christlieb N., 2005, ARA&A, 43, 531
Cayrel R. et al., 2001, Nature, 409, 691
Cayrel R. et al., 2004, A&A, 416, 1117
Cescutti G., Chiappini C., Hirschi R., Meynet G., Frischknecht U., 2013, A&A, 553, A51
Cowan J. J. et al., 2002, ApJ, 572, 861
Cowan J. J. et al., 2005, ApJ, 627, 238
Cowan J. J., Pfeiffer B, Kratz K.-L., Thielemann F.-K., Sneden C., Burles S., Tytler D., Beers T. C., 1999, ApJ, 521, 194
Cowan J. J., Rose W. K., 1977, ApJ, 212, 149
Cowan J. J., Sneden C., Lawler J. E., Aprahamian A., Wiescher M., Langanke K., Martínez-Pinedo G., Thielemann F.-K., 2021, Rev. Mod. Phys., 93, 015002
Cristiani S. et al., 2022, The Messenger, 188, 36
Dekker H., D'Odorico S., Kaufer A., Delabre B., Kotzlowski H., 2000, in Iye M., Moorwood A. F., eds, Proc. SPIE Vol. 4008, Optical and IR Telescope Instrumentation and Detectors. SPIE, Bellingham, p. 534
Del Papa D. F., Holt R. A., Rosner S. D., 2017, Atoms, 5, 5
Den Hartog E. A., Herd M. T., Lawler J. E., Sneden C., Cowan J. J., Beers T. C., 2005, The Astrophysical Journal, 619, 639
Den Hartog E. A., Lawler J. E., Roederer I. U., 2020, ApJS, 248, 10
Den Hartog E. A., Lawler J. E., Sneden C., Cowan J. J., 2003, ApJS, 148, 543
Drout M. R. et al., 2017, Science, 358, 1570
Eichler M., Sayar W., Arcones A., 2019, ApJ, 879, 47
Ernandes H. et al., 2020, in Evans C. J., Bryant J. J., Motohara K., eds, Proc. SPIE 11447, Ground-based and Airborne. Instrumentation for Astronomy VIII. SPIE, Bellingham, p. 1144760
Ernandes H., Barbuy B., Friaça A., Hill V., Spite M., Spite F., Castilho B. V., Evans C. J., 2022, MNRAS, 510, 5362(E22)
Freudling W., Romaniello M., Bramich D. M., Ballester P., Forchi V., García-Dabló C. E., Moehler S., Neeser M. J., 2013, A&A, 559, A96
Frischknecht U. et al., 2016, MNRAS, 456, 1803
Frischknecht U., Hirschi R., Thielemann F.-K., 2012, A&A, 538, L2
Fujimoto S.-i., Nishimura N., Hashimoto M.-a., 2008, ApJ, 680, 1350
Grevesse N., Sauval A. J., 1998, Space Sci. Rev., 85, 161
Gustafsson B., Edvardsson B., Eriksson K., Jørgensen U. G., Nordlund Å., Plez B., 2008, A&A, 486, 951
Hill V. et al., 2002, A&A, 387, 560
Hirai Y., Beers T. C., Chiba M., Aoki W., Shank D., Saitoh T. R., Okamoto T., Makino J., 2022, MNRAS, 517, 4856
Holmbeck E. K. et al., 2020, ApJS, 249, 30
Holmbeck E. K., Srpouse T. M., Mumpower M. R., Vassh N., Surman R., Beers T. C., Kawano T., 2019, ApJ, 870, 23
Ivans I. I., Simmerer J., Sneden C., Lawler J. E., Cowan J. J., Gallino R., Bisterzo S., 2006, ApJ, 645, 613
Just O., Bauswein A., Ardevol Pulpillo R., Goriely S., Janka H.-T., 2015, MNRAS, 448, 541
Kobayashi C. et al., 2023, ApJ, 943, L12
Kratz K.-L., Farouqi K., Pfeiffer B., Truran J. W., Sneden C., Cowan J. J., 2007, ApJ, 662, 39
Kurucz R., 1993, Kurucz CD-ROM No. 23. Smithsonian Astrophysical Observatory, Cambridge, MA
Larsen J. M., Ballester P., D'Odorico V., Ledoux C., Modigliani A., Pritchard J., Sana H., Smette A., 2007, in Kaufer A., Kerber F., eds, The 2007 ESO Instrument Calibration Workshop. Springer-Verlag, Berlin, p. 403
Lawler J. E., Bonvallet G., Sneden C., 2001a, ApJ, 556, 452
Lawler J. E., Sneden C., Cowan J. J., 2004, ApJ, 604, 850
Lawler J. E., Sneden C., Cowan J. J., 2009, ApJS, 182, 51
Lawler J. E., Wickliffe M. E., Cowley C. R., Sneden C., 2001c, ApJS, 137, 341
Lawler J. E., Wickliffe M. E., Den Hartog E. A., Sneden C., 2001b, ApJ, 563, 1075
Lawler J. E., Wyart J.-F., Blaise J., 2001d, ApJS, 137, 351
Limongi M., Chieffi A., 2018, ApJS, 237, 13
Ljung G., Nilsson H., Asplund M., Johansson S., 2006, A&A, 456, 1181
Lundqvist M., Wahlgren G. M., Hill V., 2007, A&A, 463, 693
Masterman D., Rosner S. D., Scholl T. J., Sharikova A., Holt R. O., 2003, Can. J. Phys., 81, 1389
McWilliam A., 1998, AJ, 115, 1640
McWilliam A., Wallerstein G., Mottini M., 2013, ApJ, 778, 149
Mösta P., Roberts L. F., Halevi G., Ott C. D., Lippuner J., Haas R., Schnetter E., 2018, ApJ, 864, 171
Nilsson H. et al., 2010, A&A, 511, A16
Nilsson H., Zhang Z. G., Lundberg H., Johansson S., Nordström B., 2002, A&A, 382, 368
Nishimura N., Takiwaki T., Thielemann F.-K., 2015, ApJ, 810, 109
Niu P., Liu W., Cui W., Zhang B., 2014, MNRAS, 443, 2426
Peterson R., Barbuy B., Spite M., 2020, A&A, 638, A64
Piskunov N., Kupka F., Ryabchikova T., Weiss W., Jeffery C., 1995, A&AS, 112, 525
Plez B. et al., 2004, A&A, 428, L9
Plez B., 2012, Astrophysics Source Code Library, record ascl:1205.004
Prantzos N., Abia C., Cristallo S., Limongi M., Chieffi A., 2020, MNRAS, 491, 1832
Ritter C., Herwig F., Jones S., Pignatari M., Fryer C., Hirschi R., 2018, MNRAS, 480, 538
Roederer I. U. et al., 2022a, ApJ, 936, 84
Roederer I. U. et al., 2022b, ApJS, 260, 27
Roederer I. U., Cowan J. J., Karakas A. I., Kratz K.-L., Lugaro M., Simmerer J., Farouqi K., Sneden C., 2010, ApJ, 724, 975
Roederer I. U., Hattori K., Valluri M., 2018, AJ, 156, 179
Roederer I. U., Karakas A., Pignatari M., Herwig F., 2016, ApJ, 821, 37
Roederer I. U., Kratz K.-L., Frebel A., Christlieb N., Pfeiffer B., Cowan J. J., Sneden C., 2009, ApJ, 698, 1963
Roederer I. U., Lawler J. E., 2012, ApJ, 750, 76
Rutten R. J., 1978, Sol. Phys., 56, 237
Ryabchikova T., Piskunov N., Kurucz R. L., Stempels H. C., Heiter U., Pakhomov Y., Barklem P. S., 2015, Phys. Scr., 90, 054005
Schatz H., Toenjes R., Pfeiffer B., Beers T. C., Cowan J. J., Hill V., Kratz K.-L., 2002, ApJ, 579, 638
Siegel D. M., Barnes J., Metzger B. D., 2019, Nature, 569, 241
Simmerer J., Sneden C., Cowan J. J., Collier J., Woolf V. M., Lawler J. E., 2004, ApJ, 617, 1091
Singer S., Nelder J., 2009, Scholarpedia, 4, 2928
Siqueira-Mello C. et al., 2013, A&A, 550, A122
Sneden C. et al., 2003, ApJ, 591, 936
Sneden C., Cowan J. J., Gallino R., 2008, ARA&A, 46, 241
Sneden C., Lawler J. E., Cowan J. J., Ivans I. I., Den Hartog E. A., 2009, ApJS, 182, 80
Spite F., Spite M., Barbuy B., Bonifacio P., Caffau E., François P., 2018, A&A, 611, A30
Spite M. et al., 2005, A&A, 430, 655
Tanvir N. R. et al., 2017, ApJ, 848, L27
Travaglio C., Gallino R., Armone E., Cowan J., Jordan F., Sneden C., 2004, ApJ, 601, 864
Truran J. W., 1981, A&A, 97, 391
Wahlgren G. M. et al., 2001, ApJ, 551, 520
Wanajo S., 2007, ApJ, 666, L77
Wanajo S., 2013, ApJ, 770, L22
Wanajo S., Itoh N., Ishimaru Y., Nozawa S., Beers T. C., 2002, ApJ, 577, 853
Wanajo S., Sekiguchi Y., Nishimura N., Kiuchi K., Kyutoku K., Shibata M., 2014, ApJ, 789, L39
Wiese W. L., Martin G. A., 1980, NSRDS-NBS 68, Part 2. US Government Printing Office, Washington, DC, p. 359
Winteler C., Käppeli R., Perego A., Arcones A., Vasset N., Nishimura N., Liebendörfer M., Thielemann F.-K., 2012, ApJ, 750, L22
Woosley S. E., Weaver T. A., 1995, ApJS, 101, 181

APPENDIX A: HEAVY-ELEMENT ABUNDANCES

Table A1 presents the line list of the heavy elements studied in the 3000–4000 Å region. The abundances, $\log\epsilon(\mathrm{X}) = A(\mathrm{X})$, are derived from the STIS or smoothed UVES spectra (column 4), the raw (unsmoothed) UVES spectra from the recent ESO reductions (column 5), and the Keck data (column 6); the final column of the table lists past references for each line.

Table A1. Abundances for CS 31082−001 for each near-UV, heavy-element line considered in this study. The abundances were estimated from: (a) STIS or UVES-smoothed spectra (column 4); (b) UVES-raw spectra (column 5); and (c) Keck spectra (column 6). Sources for each line are indicated in the final column, as follows: 1: Hill et al. (2002); 2: Siqueira-Mello et al. (2013); 3: Barbuy et al. (2011); 4: Cayrel et al. (2001); 5: Cowan et al. (2002); 6: Sneden et al. (2003); 7: Roederer & Lawler (2012); 8: Roederer et al. (2022b); 9: Lawler et al. (2001a); 10: Lawler et al. (2001b); 11: Lawler et al. (2001c); 12: Lawler et al. (2001d); 13: Lawler et al. (2004); 14: Den Hartog et al. (2003); 15: Nilsson et al. (2002); 16: Nilsson et al. (2010); 17: Ljung et al. (2006); 18: Wiese & Martin (1980) 19: Lawler et al. (2009): 20: Ivans et al. (2006); 21: Den Hartog et al. (2005). Symbols: [a]line not sensitive to element abundance; ':' uncertain; '::' very uncertain; ∗HFS taken into account.

λ (Å)	χ_{ex}	log *gf*	log ϵ STIS/UVES	log ϵ $\mathrm{UVES_{raw}}$	log ϵ Keck	Ref
		Ge I ($Z = 32$) $\log\epsilon(\mathrm{Ge}) = A(\mathrm{Ge}) = 0.48$				
3039.067	0.883	− 0.040	0.48	0.48	–	2
		Sr II ($Z = 38$) $\log\epsilon(\mathrm{Sr}) = A(\mathrm{Sr}) = 0.55$ – see text				
3464.453	3.040	0.530	0.37	0.40	0.40	6
3474.889	3.040	− 0.460	0.42	0.40	0.35:	18
		Y II ($Z = 39$) $\log\epsilon(\mathrm{Y}) = A(\mathrm{Y}) = -0.37$				
3095.872	0.130	− 1.740	− 0.03	− 0.03	–	8
3135.168	0.180	− 1.680	− 0.03	− 0.03	–	8
3200.272	0.130	− 0.430	− 0.23	− 0.43	–	2
3203.322	0.104	− 0.370	− 0.23	− 0.23	− 0.33	2
3216.682	0.130	− 0.020	− 0.23	− 0.43	− 0.63	2
3242.280	0.180	0.210	− 0.23	− 0.23	− 0.43	2,6
3327.878	0.409	0.130	− 0.23	− 0.43	− 0.53	6
3448.808	0.409	− 1.440	− 0.23	− 0.13	− 0.23	2
3549.005	0.130	− 0.28	− 0.23	− 0.38	− 0.43	2,5,6
3584.518	0.104	− 0.410	− 0.23	− 0.23	− 0.43	2
3600.741	0.180	0.280	− 0.23	− 0.43	− 0.43	2,5,6
3601.919	0.104	− 0.180	− 0.23	− 0.43	− 0.43	2
3611.044	0.130	0.110	− 0.23	− 0.63	− 0.53	2,5,6
3628.705	0.130	− 0.710	− 0.23	− 0.33	− 0.33	2
3633.122	0.000	− 0.100	− 0.20	− 0.63	− 0.78	2
3710.294	0.180	0.460	− 0.23	− 0.53	− 0.73	2
3747.550	0.104	− 0.910	− 0.23	− 0.43	− 0.43	5,6
3774.331	0.130	0.210	− 0.23	− 0.53	− 0.53	1,2,5,6
3788.694	0.104	− 0.070	− 0.23	− 0.43	− 0.53	1,2,5,6
3818.341	0.130	− 0.980	− 0.26	− 0.23	− 0.23	1,2,6
3832.899	0.180	− 0.340	− 0.23	− 0.53	− 0.63	6
3950.352	0.104	− 0.490	− 0.23	− 0.43	− 0.53	1,2,5,6
		Zr II ($Z = 40$) $\log\epsilon(\mathrm{Zr}) = A(\mathrm{Zr}) = 0.33$				
3019.832	0.039	− 1.130	0.43	–	–	2
3028.045	0.972	0.020	0.33	–	–	2
3030.915	0.000	− 1.040	0.43	0.33	–	2
3036.390	0.559	− 0.420	0.23	0.23	–	5
3036.514	0.527	− 0.600	0.23	0.23	–	5
3054.847	0.713	− 1.200	0.43	0.43	–	2,5,6
3060.111	0.039	− 1.370	0.43	0.03	–	5,6
3061.334	0.095	− 1.380	0.43:	0.33	–	2,5,6
3095.073	0.039	− 0.960	0.43	0.63	–	2
3125.926	0.000	− 0.883	0.43	0.43	–	2
3129.763	0.527	− 0.320	0.43	0.38	–	2
3133.489	0.959	− 0.200	0.33	0.03	–	2
3138.683	0.095	− 0.460	0.43	0.33	–	2
3231.692	0.039	− 0.590	0.43	0.38	0.63	2
3241.042	0.039	− 0.504	0.23	0.10	0.38	2
3272.221	0.000	− 0.700	0.23	0.23	0.23	2
3273.067	0.164	− 0.300	0.63:	0.63	0.63	7
3279.266	0.095	− 0.230	0.43	0.13	0.33	2
3284.703	0.000	− 0.480	0.43:	0.38	0.33	2
3305.153	0.039	− 0.690	0.43	0.33	0.48	2
3314.488	0.713	− 0.686	0.33	0.33	0.33	2
3334.607	0.559	− 0.797	0.43	0.43	0.33	2,6
3338.414	0.959	− 0.578	0.33	0.23	0.28	2,6
3340.574	0.164	− 0.461	0.43:	0.00	0.03	2
3344.786	1.011	− 0.220	0.33	0.03	0.03	17
3356.088	0.095	− 0.513	0.43:	0.33	0.43	2
3357.264	0.000	− 0.736	0.43:	0.33	0.43	2
3391.982	0.164	0.463	0.42:	0.23	0.33	2
3393.122	0.039	− 0.700	0.43	0.23	0.33	2
3402.868	1.532	− 0.330	0.23	0.23:	0.23	2
3403.673	0.999	− 0.576	0.43	0.43	0.33	2
3408.096	0.972	− 0.596	0.43	0.03	0.23	17
3410.236	0.409	− 0.323	0.23	0.23	0.03	6
3419.128	0.164	− 1.574	0.43	0.33	0.38	2
3424.813	0.039	− 1.305	0.43	0.33	0.38	2,5,6
3430.514	0.466	− 0.164	0.23	0.23	0.18	2,5,6
3438.226	0.095	0.310	0.43:	0.03	0.18	6
3457.548	0.559	− 0.530	0.43	0.43	0.43	2,5,6
3458.920	0.959	− 0.520	0.33	0.23	0.23	6
3479.029	0.527	− 0.690	0.33	0.33	0.33	2,5,6
3479.383	0.713	0.120	0.33	0.23	0.33	2,5,6
3499.560	0.409	− 0.810	0.23	0.23	0.18	2,5,6
3505.682	0.164	− 0.360	0.43:	0.33	0.23	2,5,6
3506.048	1.236	− 0.860	0.43	0.23	0.33	2
3520.869	0.559	− 1.089	0.23	0.03	0.23	2
3525.803	0.359	− 0.653	0.23	0.08	0.13	2
3536.935	0.359	− 1.306	0.33	0.33	0.28	2,5,6
3549.511	1.236	− 0.400	0.33	0.23	0.23	17
3551.939	0.095	− 0.310	0.33	0.13	0.23	2,6
3556.585	0.466	0.140	0.23	0.03	0.03	2
3573.055	0.319	− 1.041	0.43:	0.33	0.33	2,5,6
3578.205	3.033	− 1.596	0.43:	0.33	0.33	2,5,6
3588.308	0.409	− 1.130	0.43	0.33	0.33	2
3607.373	1.236	− 0.640	0.33	0.23	0.28	2
3611.889	1.743	0.450	0.23	0.23	0.03	2
3613.102	0.039	− 0.465	0.43:	–	0.23	2
3614.765	0.359	− 0.252	0.23	0.03	0.13	2
3630.004	0.359	− 1.110	0.33	0.33	0.33	2,5,6
3636.436	0.466	− 1.035	0.43	0.38	0.23	2
3674.696	0.319	− 0.446	0.33	0.23	0.13	2
3698.152	1.011	0.094	0.23	0.18	0.13	6
3714.794	0.527	− 0.930	0.63	0.53	0.53	2,5,6
3751.606	0.972	0.012	0.23	0.23	0.13	5,6
3766.795	0.409	− 0.812	0.43	0.43	0.43	2,6
3836.762	0.559	− 0.060	0.23	0.03	0.03	1
3998.954	0.559	− 0.387	0.23:	0.03	0.03	5,6
		Nb II ($Z = 41$) $\log\epsilon(\mathrm{Nb}) = A(\mathrm{Nb}) = -0.65$				
3028.433	0.439	− 0.410	− 0.55:	–	–	2
3191.093	0.514	− 0.260	− 0.55	− 0.75	–	2
3215.591	0.439	− 0.190	− 0.55	− 0.65	− 0.75	1,5,6
3225.475	0.292	− 0.030	− 0.55:	− 0.75::	− 0.65::	16
		Mo I ($Z = 42$) $\log\epsilon(\mathrm{Mo}) = A(\mathrm{Mo}) = -0.21$				
3864.103	0.000	− 0.010	− 0.11	− 0.21	− 0.24	6

Table A1 – *continued*

λ (Å)	χ_{ex}	log *gf*	log ϵ			Ref
			STIS/UVES	$UVES_{raw}$	Keck	
Ru I ($Z = 44$) $\log\epsilon(Ru) = A(Ru) = 0.18$						
3436.736	0.148	0.150	0.25	0.15	0.15	1,6
3498.942	0.000	0.310	0.25	0.15	0.15	1,6
3728.025	0.000	0.270	0.25	0.20	0.20	1,6
3798.898	0.148	−0.040	0.25:	0.20	0.20	1,6
3799.349	0.000	0.020	0.36:	0.20	0.20	1,6
Rh I ($Z = 45$) $\log\epsilon(Rh) = A(Rh) = -0.51$						
3396.819	0.000	0.050	−0.42	−0.62	−0.42	1
3434.885	0.000	0.450	−0.42	−0.57	−0.52	1,6
3692.358	0.000	0.174	−0.42	−0.42	−0.52	1,6
3700.907	0.190	−0.100	−0.42	−0.42:	−0.52:	2
Pd I ($Z = 46$) $\log\epsilon(Pd) = A(Pd) = -0.21$						
3242.700	0.814	−0.070	−0.05	−0.15	−0.15	1,5,6
3404.579	0.814	0.320	−0.20	−0.35	−0.35	1,5,6
3460.739	0.814	−0.420	−0.15	−0.20	−0.20	6
3516.944	0.962	−0.240	−0.05	−0.20	−0.10	2,5,6
3634.690	0.814	0.090	−0.05	−0.15	−0.05	1
Ag I ($Z = 47$) $\log\epsilon(Ag) = A(Ag) = -0.94$						
3280.679	0.000	−0.050	−1.01	−1.01	−0.96	1,5,6
3382.889	0.000	−0.377	−0.91	−0.87	−0.91	1,5,6
Cd I ($Z = 48$) $\log\epsilon(Cd) = A(Cd) =$ –						
3261.050	0.000	−2.470	–	–	–	6
Sn I ($Z = 50$) $\log\epsilon(Sn) = A(Sn) = <-0.40$						
3262.331	1.068	0.110	−0.90	< −0.40	–	6
3655.790	2.128	−0.450	–	...		
3801.011	1.068	−0.620	–	6		
Ba II ($Z = 56$) $\log\epsilon(Ba) = A(Ba) = 0.40$ – see text						
3891.776*	2.512	0.280	+0.15	+0.15	0.00	1,5,6
La II ($Z = 57$) $\log\epsilon(La) = A(La) = -0.73$						
3713.545*	0.173	−0.800	−0.60	−0.60	−0.60	5,6,9
3794.774*	0.244	−0.443	−0.60	−0.80	−0.90	5,6,9
3849.006*	0.000	−0.450	−0.60	−0.75	−0.80	1,5,9
3949.102*	0.403	−1.690	−0.80	−0.80	−0.60	5,6,9
3988.515*	−1.015	0.210	−0.70	−0.70	−0.70	5,6,9
3995.745*	−1.109	0.060	−0.60	−0.75	−0.70	5,6,9
Ce II ($Z = 58$) $\log\epsilon(Ce) = A(Ce) = -0.41$						
3263.885	0.459	−0.390	–	–	–	19,2
3426.205	0.122	−0.660	−0.31	−0.31	−0.41	2,6,19
3507.941	0.175	−0.960	−0.31	−0.15	−0.31	2,19
3520.520	0.175	−0.910	−0.31	−0.25	−0.31	2,19
3534.045	0.521	−0.140	−0.31	−0.36	−0.26	2,19
3539.079	0.320	−0.270	−0.31	−0.41	−0.41	2,5,6,19
3577.456	0.470	0.140	−0.31	−0.41	−0.31	2,5,6,19
3655.844	0.318	−0.050	−0.31	−0.41	−0.46	6,19
3659.225	0.175	−0.670	−0.31	−0.41	−0.36	2,19
3709.929	0.122	−0.260	−0.31	−0.41	−0.41	2,19
3781.616	0.529	−0.260	−0.31	−0.41	−0.36	2,19
3940.330	0.318	−0.270	−0.31	−0.41	−0.36	5,6,19
3940.660	0.495	−0.991	−0.31	–	–	19
3940.970	0.417	−0.570	−0.31	–	–	19
3942.151	0.000	−0.220	−0.31	−0.41	−0.41	5,6,19
3942.745	0.857	0.690	−0.31	−0.61	−0.61	5,6,19
3960.909	0.322	−0.360	−0.31	−0.41	−0.41	5,6,19
3964.496	0.322	−0.650	−0.31	−0.51	−0.61	6,19

Table A1 – *continued*

λ (Å)	χ_{ex}	log *gf*	log ϵ			Ref
			STIS/UVES	$UVES_{raw}$	Keck	
3984.671	0.956	0.000	–	–	–	6,19
3992.380	0.446	−0.220	−0.31	−0.41	−0.41	6,19
3999.237	0.090	0.060	–	−0.61	–	5,6
Pr II ($Z = 59$) $\log\epsilon(Pr) = A(Pr) = -0.94$						
3964.262*	0.215	−0.230	−0.86	–	–	1
3964.812*	0.055	−0.920	−0.86	−0.96	−0.96	1,5,6
3965.253*	0.204	−0.854	−0.86	−0.91	−0.91	1,5,6
Nd II ($Z = 60$) $\log\epsilon(Nd) = A(Nd) = -0.33$						
3285.085	0.000	−1.050	–	–	–	2
3300.143	0.000	−1.036	−0.13	−0.33	−0.33	2
3325.889	0.064	−1.174	−0.13	−0.23	−0.13	2
3334.465	0.182	−0.930	–	–	–	2
3555.764	0.321	−0.950	−0.13	−0.23	−0.23	2
3560.718	0.471	−0.500	−0.13	−0.33	−0.43	2
3598.021	0.064	−1.020	−0.13	−0.23	−0.18	2
3609.780	0.000	−0.800	−0.13	−0.28	−0.33	2
3730.577	0.380	−0.611	−0.13	−0.20	−0.23	2
3738.055	0.559	−0.040	−0.13	−0.23	−0.23	2
3741.424	0.064	−0.680	−0.13	−0.33	−0.33	2
3763.472	0.205	−0.430	−0.13	−0.23	−0.33	2
3779.462	0.182	−0.560	−0.13	−0.33	−0.33	2
3780.382	0.471	−0.350	−0.13	−0.23	−0.33	2,5,6
3784.245	0.380	0.150	−0.13	−0.33	−0.33	2,5,6
3795.454	0.205	−0.650	−0.13	−0.28	−0.28	2
3803.471	0.205	−0.390	−0.13	−0.33	−0.33	2
3808.767	0.064	−0.650	−0.13	−0.53	−0.53	2
3810.477	0.742	−0.140	−0.13	−0.38	−0.33	14
3826.409	0.064	−0.410	−0.13	−0.33	−0.33	5,6
3838.981	0.000	−0.240	−0.13	−0.43	−0.48	5,6
3865.956	0.380	−1.048	−0.13	−0.43	−0.43	5,6
3866.791	0.205	−0.950	−0.13	−0.53	−0.53	6
3900.219	0.471	0.100	−0.13	−0.33	−0.33	5,6
3973.260	0.631	0.360	−0.13	−0.43	−0.43	1,5,6
Sm II ($Z = 62$) $\log\epsilon(Sm) = A(Sm) = -0.54$						
3218.596	0.185	−0.793	−0.51	−0.31	−0.51	2
3244.686	0.185	−1.399	−0.11:	−0.21:	–	2
3253.403	0.104	−1.080	−0.31	−0.31	−0.31	2
3304.517	0.000	−1.190	−0.51	−0.51	−0.51:	2
3307.027	0.659	−0.301	−0.11	−0.21	−0.11	2
3321.189	0.378	−0.362	−0.51	−0.51	−0.51	2
3384.654	0.378	−0.741	−0.51	−0.61	−0.46	2
3568.271	0.485	0.298	−0.51	−0.51	−0.71	2
3583.372	0.185	−1.119	−0.51	−0.51	−0.31	2
3604.281	0.485	−0.158	−0.51	−0.51	−0.41	2
3609.492	0.277	0.160	−0.71	−0.81	−0.71	2
3621.210	0.104	−0.442	−0.51	−0.91	−0.71	2
3627.004	0.277	−0.614	−0.51	−0.51	−0.51	2
3661.352	0.041	−0.427	−0.51	−0.91	−0.71	2
3670.821	0.104	−0.344	−0.51	−0.71	−0.71	2
3706.752	0.485	−0.600	−0.51	−0.51	−0.51	2,6
3718.883	0.378	−0.310	−0.51	−0.61	−0.91	2
3731.263	0.104	−0.384	−0.51	−0.71	−0.61	2
3739.120	0.041	−0.846	−0.51	−0.41	−0.51::	2
3743.877	0.333	−0.428	−0.51	−0.51	−0.41	2
3758.460	0.000	−1.102	−0.51	−0.31	−0.71	2
3760.710	0.185	−0.428	−0.51	−0.61	−0.51	2,6
3762.588	0.248	−0.751	−0.51	−0.61	−0.61	2
3793.978	0.104	−0.498	−0.63	−0.58	−0.71	1
3896.972[a]	0.041	−0.578	−0.51	−0.51	−0.71	1,5,6
3993.309	0.041	−0.894	−0.51	−0.51	−0.61	6
Eu II ($Z = 63$) $\log\epsilon(Eu) = A(Eu) = -0.93$						
3688.430*	0.000	−0.670	−0.76	−0.96	−1.16	10,20
3724.930*	0.000	−0.090	−0.76	−0.76	−0.86	1,5,6,10,20
3819.672*	0.000	0.510	−0.76	−0.96	−0.96	5,6,10,20

Table A1 – *continued*

λ (Å)	χ_{ex}	log *gf*	log ϵ			Ref
			STIS/UVES	$UVES_{raw}$	Keck	
3907.107*	0.207	0.170	− 0.76	− 0.96	− 0.96	5,6,10,20
3930.499*	0.207	0.270	− 0.76	− 0.96	− 0.86	1,5,6,10,20
3971.972*	0.207	0.270	− 0.86	− 0.96	− 0.96	1,5,6,10,20
Gd II ($Z = 64$) $\log\epsilon(\mathrm{Gd}) = A(\mathrm{Gd}) = -0.45$						
3032.844	0.079	0.300	− 0.47	–	–	8
3034.051	0.032	0.149	− 0.47:	–	–	8
3076.928	0.000	− 0.480	− 0.27	− 0.27	–	8
3100.504	0.240	0.620	− 0.27	− 0.42	–	8
3124.262	0.032	− 1.250	− 0.27	− 0.47	–	8
3331.387	0.000	− 0.140	− 0.27	− 0.47	− 0.57	5,6
3358.625	0.032	0.152	− 0.27	− 0.27	− 0.27	2
3360.712	0.032	− 0.240	–	–	–	2
3362.239	0.079	0.294	− 0.27	− 0.37	− 0.57:	2
3364.245	0.000	− 1.086	− 0.27	− 0.57	− 0.67:	2
3392.527	0.079	− 0.220	− 0.27	− 0.47	− 0.47	2
3418.729	0.000	− 0.310	− 0.27	− 0.47	− 0.47	2
3422.464	0.240	0.519	+0.03	− 0.77	− 0.27	2
3423.924	0.000	− 0.520	− 0.27	− 0.37	− 0.47	2
3424.595	0.354	− 0.170	− 0.27	− 0.47	− 0.47	6
3439.208	0.382	0.150	− 0.42	− 0.47	− 0.47	2,5,6
3439.787	0.425	− 0.230	− 0.12	− 0.27	− 0.17	2
3439.988	0.240	0.100	− 0.12	− 0.27	− 0.17	2
3451.236	0.382	− 0.050	− 0.47	− 0.57	− 0.47	2,5,6
3454.907	0.032	− 0.480	− 0.27	− 0.47	− 0.52	2,6
3463.990	0.427	0.269	− 0.27	− 0.47	− 0.27	2
3467.274	0.425	0.064	− 0.27	− 0.47	− 0.52	2
3473.224	0.032	− 0.412	− 0.27	− 0.27	− 0.27	2
3481.802	0.492	0.230	− 0.27	− 0.47	− 0.47	2
3482.607	0.427	− 0.484	–	–	–	2
3491.960	0.000	− 0.611	− 0.27	− 0.27	− 0.22	2
3549.359	0.240	0.260	− 0.27	− 0.47	− 0.47	5,6
3557.058	0.600	0.210	− 0.27	− 0.47	− 0.47	2,5,6
3646.196	0.240	0.328	− 0.27	− 0.47	− 0.47	2
3654.624	0.079	− 0.030	− 0.27	− 0.47	− 0.47	2
3656.152	0.144	− 0.067	− 0.27	− 0.42	− 0.47	2
3671.205	0.079	− 0.330	− 0.27	− 0.47:	− 0.67	2
3697.733	0.032	− 0.280	− 0.27	− 0.37	− 0.27	5,6
3699.737	0.354	− 0.260	− 0.27	− 0.47	− 0.47	2
3712.704	0.382	0.150	− 0.47	− 0.57	− 0.57	5,6
3768.396	0.079	0.360	− 0.27	− 0.57	− 0.57	1,5,6
3796.384	0.032	0.14	− 0.27	− 0.47	− 0.47	1,6
3836.915	0.492	− 0.322	− 0.27	− 0.47	− 0.37	1
3844.578	0.144	− 0.400	− 0.27	− 0.37	− 0.37	1,5,6
3916.509	0.600	0.060	− 0.27	− 0.47	− 0.47	1
3973.977	0.602	− 0.400	− 0.47	− 0.57	− 0.67	6
Tb II ($Z = 65$) $\log\epsilon(\mathrm{Tb}) = A(\mathrm{Tb}) = -1.22$						
3070.060	0.400	0.170	− 1.26	− 1.00	–	8
3472.800*	0.126	− 0.10	− 1.26:	− 1.26:	− 1.36:	6,11,12
3509.144	0.000	0.700	− 1.26	− 1.26	− 1.26	2,11,12
3568.510*	0.000	− 1.928	− 1.26	− 1.26	− 1.26	1,6,11,12
3600.410*	0.641	− 1.519	− 1.26	− 1.26	− 1.16	5,6,11,12
3633.287	0.641	0.090	− 1.26:	− 1.26:	− 1.26:	2,11,12
3641.655	0.649	0.040	− 1.26:	− 1.26:	− 1.26:	2,11,12
3658.886*	0.126	− 4.083	− 1.26	− 1.26	− 1.26	1,5,6,11,12
3702.853*	0.126	− 1.794	− 1.26	− 1.26	− 1.16	1,5,6,11,12
3848.734*	0.000	− 2.008	− 1.26	− 1.26	− 1.26	1,5,6,11,12
3874.168*	0.000	− 0.317	–	− 1.15	− 1.26	1,5,6,11,12
3899.188	0.373	0.330	− 1.26	− 1.15	− 1.00	1,11,12
Dy II ($Z = 66$) $\log\epsilon(\mathrm{Dy}) = A(\mathrm{Dy}) = -0.25$						
3026.160	0.000	− 0.980	− 0.50	–	–	8
3407.796	0.000	0.180	− 0.21	− 0.21	− 0.21	2,5,6
3413.784	0.103	− 0.460	− 0.21	− 0.21	− 0.21	2
3434.369	0.000	− 0.450	− 0.21	− 0.21	− 0.21	2,5,6
3445.574	0.000	− 0.150	− 0.21	− 0.21	− 0.21	5,6
3449.892	0.538	− 0.524	− 0.21	− 0.41	− 0.26	6
3454.317	0.103	− 0.140	− 0.21	− 0.21	− 0.41	2,5,6

Table A1 – *continued*

λ (Å)	χ_{ex}	log *gf*	log ϵ			Ref
			STIS/UVES	$UVES_{raw}$	Keck	
3456.559	0.590	− 0.007	− 0.21	− 0.41	− 0.41	2
3460.969	0.000	− 0.070	− 0.21	− 0.21	− 0.31	2,5,6
3473.697	0.928	− 0.218	− 0.21	− 0.41	− 0.41	6
3506.815	0.103	− 0.440	− 0.21	− 0.36	− 0.36	6
3531.707	0.000	0.790	− 0.21	− 0.21	− 0.41	2,6
3534.960	0.103	− 0.040	− 0.21	− 0.21	− 0.21	2
3536.019	0.538	0.530	− 0.21	− 0.21	− 0.41	2,5,6
3538.519	0.000	− 0.020	− 0.21	− 0.11	− 0.21	5,6
3546.832	0.103	− 0.550	− 0.21	− 0.21	− 0.21	2,5,6
3550.218	0.590	0.270	− 0.21	− 0.36	− 0.31	2,5,6
3559.295	1.224	− 0.280	− 0.21	− 0.21	− 0.41	5,6
3563.148	0.103	− 0.360	− 0.21	− 0.21	− 0.21	2,5,6
3640.249	0.590	− 0.370	− 0.21	− 0.21	− 0.31	6
3694.810	0.103	− 0.110	− 0.21	− 0.21	− 0.41	2,5,6
3708.221	0.590	− 0.880	− 0.21	− 0.21	− 0.21	6
3747.817	0.103	− 0.810	− 0.21	− 0.21	− 0.21	5,6
3788.436	0.103	− 0.570	− 0.21	− 0.21	− 0.21	5,6
3869.864	0.000	− 1.050	− 0.21	− 0.21	− 0.26	1
3944.681	0.000	0.100	− 0.21	− 0.36	− 0.21	7
3983.651	0.538	− 0.310	− 0.21	− 0.21	− 0.21	5,6
3996.689	0.590	− 0.260	− 0.21	− 0.21	− 0.21	1,5,6
Ho II ($Z = 67$) $\log\epsilon(\mathrm{Ho}) = A(\mathrm{Ho}) = -0.98$						
3796.748*	0.000	0.160	− 1.0	− 0.96	− 0.96	13
3810.738*	0.000	0.190	− 0.9	− 0.91	− 0.91	5,6,13
3890.925*	− 0.293	0.460	− 1.0	− 1.06	− 1.06	5,13
3905.634	0.079	− 0.530	–	–	–	6,13
Er II ($Z = 68$) $\log\epsilon(\mathrm{Er}) = A(\mathrm{Er}) = -0.38$						
3028.275	0.00	1.02	–	–	–	8
3073.344	0.000	− 0.610	− 0.42	− 0.47	–	8
3332.703	0.886	0.041	− 0.27	− 0.47	–	6
3364.076	0.055	− 0.487	− 0.32	− 0.42	− 0.27	2
3441.130	0.055	− 0.672	− 0.27	− 0.27	− 0.27	2
3499.103	0.055	0.139	− 0.27	− 0.47	− 0.47	2,5
3524.913	0.000	− 0.887	− 0.27	− 0.37	− 0.37	2
3549.844	0.670	− 0.310	− 0.27	− 0.47	− 0.47	2
3559.894	0.000	− 0.736	− 0.32	− 0.37	− 0.37	2,5,6
3580.518	0.055	− 0.768	− 0.27	− 0.27	− 0.27	2
3616.566	0.000	− 0.327	− 0.27	− 0.27	− 0.27	2
3618.916	0.670	− 0.594	− 0.27	− 0.07:	− 0.27:	2
3633.536	0.000	− 0.694	− 0.27	− 0.37	− 0.42	2
3692.649	0.055	0.138	− 0.27	− 0.37	− 0.37	1,2,5,6
3700.720	0.055	− 1.290	− 0.27	− 0.27	− 0.27	2
3729.524	0.000	− 0.488	− 0.37	− 0.47	− 0.47	2,6
3742.640	0.636	− 0.474	− 0.27	− 0.47	− 0.47	2
3786.836	0.000	− 0.644	− 0.27	− 0.27	− 0.47	1,2,5
3830.482	0.000	− 0.365	− 0.27	− 0.42	− 0.47	1,5
3896.234	0.055	− 0.241	− 0.27	− 0.42	− 0.42	1,5
3906.312	0.000	− 0.052	− 0.27	− 0.47	− 0.47	7
3938.626	0.000	− 0.520	− 0.27	− 0.47	− 0.47	1,5,6
Tm II ($Z = 69$) $\log\epsilon(\mathrm{Tm}) = A(\mathrm{Tm}) = -1.32$						
3015.294	0.029	− 0.590	− 1.24	–	–	2
3131.255	0.000	0.240	− 1.24	− 1.44	–	2
3362.615	0.029	− 0.100	− 0.89:	− 1.04	− 1.04	2
3397.498	0.000	− 0.750	− 1.24	− 1.24	− 1.14	2
3462.197	0.000	0.030	− 1.24	− 1.39	− 1.34	2,6
3700.256	0.029	− 0.290	− 1.24	− 1.24	− 1.24	1,2,5,6
3701.363	0.000	− 0.540	− 1.24	− 1.24	− 1.04	2,6
3761.914	0.000	− 0.430	− 1.39	− 1.64	− 1.54	1,2,6
3795.760	0.029	− 0.230	− 1.24	− 1.29	− 1.34	1,2,6
3848.020	0.000	− 0.130	− 1.24	− 1.39	− 1.34	1,5,6
Yb II ($Z = 70$) $\log\epsilon(\mathrm{Yb}) = A(\mathrm{Yb}) = -0.70$						
3289.367*	0.000	− 0.050	− 0.65	− 0.70	− 0.40	6,19
3694.192*	5.724	− 0.200	− 0.70	− 0.70	− 0.85	6,19

Table A1 – *continued*

λ (Å)	χ_{ex}	log *gf*	log ϵ STIS/UVES	log ϵ $UVES_{raw}$	log ϵ Keck	Ref
		Lu II ($Z = 71$)				
		$\log\epsilon(Lu) = A(Lu) = -1.14$				
3077.605*	1.541	− 0.653	− 1.14	− 1.14	–	2
3397.066*	1.462	− 1.006	− 1.14	− 1.14	− 0.94	6
3472.477*	1.541	− 1.412	–	–	–	6
3554.416*	2.148	− 0.898	–	–	–	6
		Hf II ($Z = 72$)				
		$\log\epsilon(Hf) = A(Hf) = -0.88$				
3012.900	0.000	− 0.600	− 0.59	–	–	2
3109.113	0.787	− 0.250	− 0.59	− 0.89	–	2
3255.279	0.452	− 1.130	− 0.59	− 0.89	− 0.74	2
3399.793	0.000	− 0.570	− 0.89	− 0.95	− 0.89	1,2
3569.034	0.787	− 0.400	− 0.59	− 0.89	− 0.89	2
3719.276	0.608	− 0.810	− 0.59	− 0.89	− 0.89	1,6
3793.379	0.378	− 1.110	–	− 0.79:	− 0.84	6
		Os I ($Z = 76$)				
		$\log\epsilon(Os) = A(Os) = 0.23$				
3018.036	0.000	− 0.720	0.10	–	–	5
3058.655	0.000	− 0.451	0.30	0.10	–	2,3,5,6
3267.945	0.000	− 1.080	0.20	0.10	0.10	5,6
3301.565	0.000	− 0.743	0.20	0.20	0.15	5,6
3528.598	0.000	− 1.740	–	0.50	0.30	6
		Ir I ($Z = 77$)				
		$\log\epsilon(Ir) = A(Ir) = 0.10$				
3047.158	1.623	− 0.500	0.20:	–	–	3
3220.776	0.352	− 0.510	0.50:	0.30:	0.40:	5
3513.648	0.000	− 1.260	0.20	0.10	0.20	1,5,6
3558.993	0.717	− 1.670	0.00	0.00	0.00	6
3800.120	0.000	− 1.450	0.20	0.00	0.20	1,5,6
		Pt I ($Z = 78$)				
		$\log\epsilon(Pt) = A(Pt) = 0.0$ (see text)				
3064.711*	0.000	− 0.340	− 0.50	− 0.50	–	5,21
3139.387	0.100	− 1.580	0.50	0.50	–	8
3301.859*	0.814	− 0.770	− 1.10	− 1.10	− 1.10	6,21
3315.042	0.000	− 2.580	0.50	0.50	–	6
		Pb I ($Z = 82$)				
		$\log\epsilon(Pb) = A(Pb) = -0.65$ (see text)				
3639.568	0.969	− 0.720	–	–	–	5
3683.462	0.969	− 0.600	–	–	–	5,6
		Bi I ($Z = 83$)				
		$\log\epsilon(Bi) = A(Bi) = -0.20$ (see text)				
3024.635	1.914	− 0.15	− 0.20	–	–	3
3067.707	0.000	0.220	–	–	–	3
		Th II ($Z = 90$)				
		$\log\epsilon(Th) = A(Th) = -1.04$				
3180.194	0.189	− 0.547	–	–	–	15
3351.229	0.188	− 0.600	− 0.98	− 0.98	− 0.98	1
3433.999	0.230	− 0.537	− 0.98	− 1.18	− 1.08	1
3435.977	0.000	− 0.670	− 0.98	− 1.10	− 0.78	1
3469.921	0.514	− 0.129	− 0.98	− 1.00	− 0.98	1
3539.587	0.000	− 0.760	− 0.98	− 0.98	− 0.98	15
3675.567	0.188	− 0.840	− 0.98	− 0.98	− 0.98	1
		U II ($Z = 92$)				
		$\log\epsilon(U) = A(U) = -1.92$				
3859.577	0.036	− 0.067	–	–	–	1,4,5,6

APPENDIX B: CS 31082−001 AT THE RESOLUTION OF CUBES

The CUBES instrument is designed to deliver a spectral resolving power of $R \gtrsim 20\,000$ in its high-resolution mode, yielding FWHM ~ 0.136 Å with a minimum of 2.3-pixel sampling, in the near-IV region. Assuming a 2.3–2.7-pixel sampling in the design, this corresponds to half the sampling obtained with UVES of 5 pixels per resolution element. The goal for the wavelength coverage is from 3000 up to 4050 Å, with an overview of the instrument given by Cristiani et al. (2022).

CUBES will be installed at the Cassegrain focus of one of the Unit Telescopes of the VLT. The design features a two-channel spectrograph fed by an image slicer (with six slices) yielding two complementary spectra from 3000–3520 and 3460–4050 Å in two CCD detectors. The estimated efficiency of CUBES should enable observations of stars with $V\sim18.0$, considerably expanding the sample of metal-poor stars observable in the near-UV.

Initial simulations of CUBES observations were presented by Ernandes et al. (2020) to explore the parameter space of the instrument design. These first simulations were applied to red giant and dwarf models with metallicities of [Fe/H] = −1.0 and −3.0. From their results the new elements reported here for CS 31082−001 (Ho and Yb) appear feasible with CUBES.

To illustrate the potential of CUBES for some of the other elements studied here, in Fig. B1, we show simulated CUBES observations of the Dy II 3434.369 Å and Os I 3267.945 Å lines with $R = 22\,000$, binned and recomposed through the end-to-end simulator (upper panels); the UVES spectra convolved to $R = 22\,000$ and with a half number of points corresponding to 2.5 pixels per resolution element (middle panels); compared with the UVES data (lower panels), and demonstrating comparably good constraints on the estimated abundances.

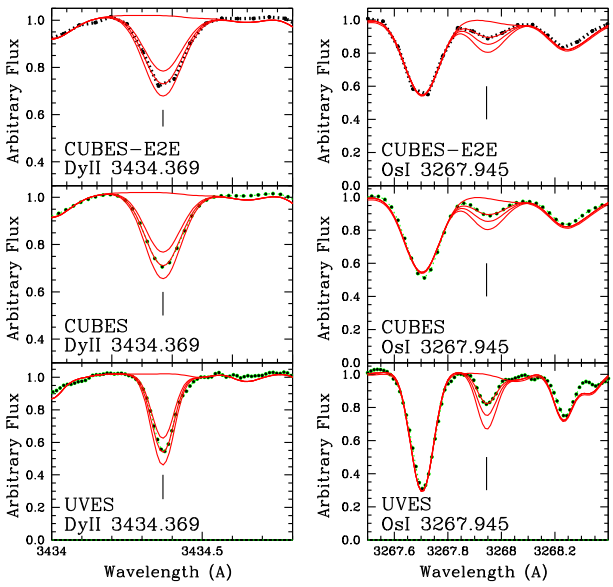

Figure B1. Simulated CUBES observations of CS 31082−001 for the Dy II 3434.369 Å and Os I 3267.945 Å lines binned and recomposed through the end-to-end simulator (upper panels); $R = 22\,000$, 2.5 pixels per resolution element (middle panels), compared with the UVES data considered in this study (lower panels). The abundances are A(Dy)=none,−0.41, −0.21, −0.01 (left-hand panels), and A(Os) = none, 0.1, 0.3, 0.5 (right-hand panels).

APPENDIX C: THE MEAFS CODE

We have gone through line-by-line fitting manually for the present results. In parallel, we are developing the MEAFS code, created to automatically derive abundances with high precision for the lines that permit this treatment; a more detailed description will be given in a future publication. This optimized script is coded in PYTHON with the key functions coded in C. The code generates synthetic spectra using a stellar spectral-synthesis software to automatically fit the best set of parameters using the Nelder–Mead (Singer & Nelder 2009) method to fit an observed spectrum. Our tests here of the MEAFS code for automatic, efficient, and precise measurements, have validated it for clear and unblended lines, as illustrated in Fig. C1.

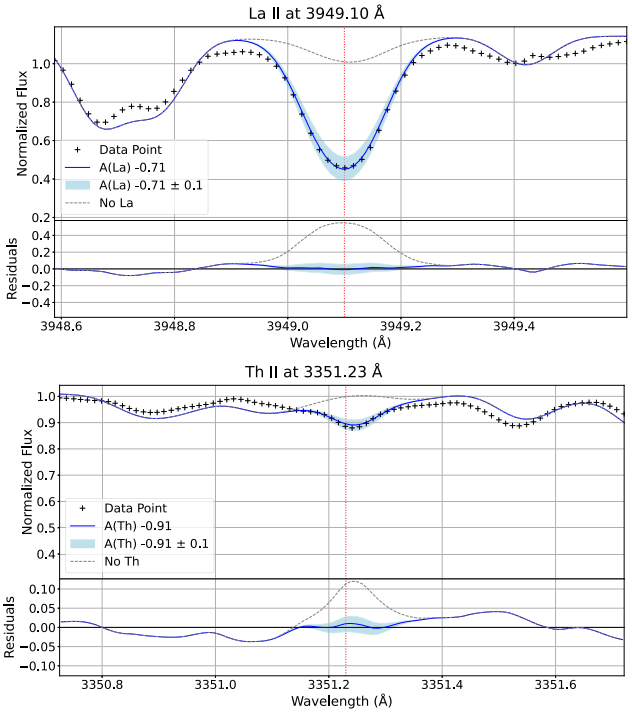

Figure C1. Fits of the La II 3949.10 Å and Th II 3351.23 Å lines using the MEAFS code.

This paper has been typeset from a TEX/LATEX file prepared by the author.